ADVANCED MATERIALS
www.advmat.de

Nanoplastics: Immune Impact, Detection, and Internalization after Human Blood Exposure by Single-Cell Mass Cytometry

Laura Fusco, Arianna Gazzi, Linda Giro, Roman B. Schefer, Sènan Mickael D'Almeida, Roberta Cagliani, Martina Zoccheddu, Recep Uyar, Ömur Besbinar, Doğantan Çelik, Acelya Yilmazer, Denise M. Mitrano, Marco Orecchioni,* and Lucia Gemma Delogu**

The increasing exposure to nanoplastics (NPs) raises significant concerns for human health, primarily due to their potential bioaccumulative properties. While NPs have recently been detected in human blood, their interactions with specific immune cell subtypes and their impact on immune regulation remain unclear. In this proof-of-concept study, model palladium-doped polystyrene NPs (PS-Pd NPs) are utilized to enable single-cell mass cytometry (CyTOF) detection. The size-dependent impact of carboxylate polystyrene NPs (50–200 nm) is investigated across 15 primary immune cell subpopulations using CyTOF. By taking advantage of Pd-doping for detecting PS-Pd NPs, this work evaluates their impact on human immune-cells at the single-cell level following blood exposure. This work traces PS-Pd NPs in 37 primary immune-cell subpopulations from human blood, quantifying the palladium atom count per cell by CyTOF while simultaneously assessing the impact of PS-Pd NPs on cell viability, functionality, and uptake. These results demonstrate that NPs can interact with, interfere with, and translocate into several immune cell subpopulations after exposure. In vivo distribution experiments in mice further confirmed their accumulation in immune cells within the liver, blood, and spleen, particularly in monocytes, macrophages, and dendritic cells. These findings provide valuable insights into the impact of NPs on human health.

1. Introduction

The worldwide plastic waste generation has increased exponentially in the last 50 years,[1–3] resulting in the ubiquitous distribution of plastic debris through environmental transport and deposition.[4–8] These plastic items undergo fragmentation, leading to the unintentional formation of microplastics and nanoplastics (NPs smaller than 1 µm in diameter).[9–11] Due to their persistence, their presence in the environment is becoming a global problem that may impact human health in a variety of ways.[12–14] In the last years, a large amount of literature has reported the impact of NPs on various ecosystems,[15–18] as well as their abundance in drinking water,[19] urban air,[20,21] and food.[22–24] Recently, NPs were found in the human bloodstream.[25] Since the immune system controls the susceptibility to foreign molecules, understanding its perturbations is a fundamental step for the toxicological evaluation of NPs.

L. Fusco, A. Gazzi, L. Giro, R. Cagliani, L. G. Delogu
ImmuneNano-lab
Department of Biomedical Sciences
University of Padua
Padua 35131, Italy
E-mail: luciagemma.delogu@unipd.it
L. Giro, M. Zoccheddu, M. Orecchioni
Immunology Center of Georgia
Augusta University
Augusta 30912, United States
E-mail: morecchioni@augusta.edu

The ORCID identification number(s) for the author(s) of this article can be found under https://doi.org/10.1002/adma.202413413

© 2024 The Author(s). Advanced Materials published by Wiley-VCH GmbH. This is an open access article under the terms of the Creative Commons Attribution-NonCommercial License, which permits use, distribution and reproduction in any medium, provided the original work is properly cited and is not used for commercial purposes.

DOI: 10.1002/adma.202413413

R. B. Schefer, D. M. Mitrano
Department of Environmental Systems Science
ETH Zürich
Zürich 8092, Switzerland
S. M. D'Almeida
Flow Cytometry Core Facility
School of Life Sciences
EPFL
Lausanne 1015, Switzerland
M. Zoccheddu
Georgia Cancer Center Integrated Genomics core
Augusta University
Augusta 30912, United States
R. Uyar, Ö. Besbinar, D. Çelik, A. Yilmazer
Stem Cell Institute
Ankara University
Ankara 06100, Turkey
E-mail: acelya.yilmazer.aktuna@ankara.edu.tr

Considering the variability of the results obtained in animal models[26] and the lack of the translational impact of in vitro studies (performed in mouse or human immortalized cell lines),[27–29] the interaction of NPs with primary human immune cells and their potential immunotoxicity after blood contamination is still unknown.[30] In particular, it remains to be elucidated whether they are carried by specific immune cell types and potentially affect immune regulation, which could enhance the predisposition to diseases with an immunological base. In addition, so far, only limited in vitro studies on plastic pollutants investigating the effect elicited by micro and nano-sized particles have been carried out, preventing conclusions on size-dependent effects.[28,29,31] According to a recent publication, PS microplastics with diameters ranging from 10 to 100 µm did not exhibit significant toxicity to human immune cells at a concentration of 500 µg mL^{-1}.[32]

To evaluate the effects of NPs and the risks to human health, it is essential to understand their fate in biological systems.[33] To date, different studies have aimed at assessing the effects and biodistribution of PS NPs using Raman imaging[34] or incorporating isotopes[35,36] and fluorescent tracers in the NPs.[37–42] However, these techniques do not allow the simultaneous detection of multiple cell types and parameters along with the NPs. In addition, fluorescent labeling and imaging suffer different drawbacks. The background fluorescence that most organisms have and the quenching of fluorescent signals in harsh conditions may affect the sensitivity and accuracy of detection.[43] Moreover, recently published studies demonstrated that dye could leach from NPs and reach biological tissue without plastic, leading to misinterpretations of the results.[44,45] To overcome this limitation in NP tracking, model metal-doped NPs containing palladium (Pd) were reported to allow NP detection via inductively coupled plasma mass spectrometry (ICP-MS) with high sensitivity and specificity.[43,46–50] However, a strategy to simultaneously detect NPs while revealing their impact and interaction with the complexity of human immune cells on 30 different subpopulations is still missing.[51] In particular, it has recently been demonstrated that plastic particles are bioavailable for uptake into the human bloodstream from environmental exposure[25] by applying chromatography/mass spectrometry to measure plastic particles ≥700 nm in human whole blood. Following blood exposure, plastic particles exert toxic effects and interfere with the immune cells present in the bloodstream. However, understanding the associated hazards of such exposure is still required to determine the possible public health risk.

To shed light on this aspect, here, we used carboxylate polystyrene nanoparticles (PS NPs), with diameters ranging from 50 to 200 nm, to evaluate the size-dependent impact of NPs on fifteen primary human immune cells. Moreover, we studied their effects after blood exposure by single-cell mass cytometry (CyTOF),[52] a crucial and innovative technology to decipher the biological impact of various agents in depth.[53–58] We introduced the use of CyTOF to assess the impact of NPs on immune cells and detect if and to what extent they can be localized in the different PBMC subpopulations. We exploited model Pd-doped polystyrene NPs (PS-Pd),[46] which we previously designed for excellent NP tracking,[46,51] to enable Pd detection by using the metal as a proxy for the plastic. In this context, we applied our recently introduced LINKED approach[58] to study the NP's impact on human health. By taking advantage of single-cell mass cytometry, we deepened our understanding of the effects of NPs on 30 different primary immune cell subpopulations from human whole blood by quantifying the number of Pd atoms per cell by CyTOF and interrogating several biological parameters. Our study gives a broad view of NP effects on cell viability, functionality, and cell uptake on whole blood immune subpopulations by CyTOF (**Figure 1**).

2. Results and Discussion

2.1. Nanoplastic Characterization

We employed two model NPs, namely PS NPs of different sizes purchased by Polysciences GmbH and PS-Pd NPs. We synthesized the latter according to our published procedures[46] and conducted a thorough physicochemical characterization of PS-Pd NPs. As shown in Figure S1a, Supporting Information, the particles had an average size of 210 nm ± 26 nm and had a smooth surface (Figure S1b, Supporting Information). As particle size is integral to the potential for particle uptake and interaction with cells, both PS NPs and PS-Pd NPs (500 µg mL^{-1}) were incubated at 37 °C in water or RPMI 1640 culture media supplemented with 10% fetal bovine serum (FBS) to assess agglomeration over the exposure period. The evaluation was carried out utilizing Dynamic Light Scattering (DLS), interpreting alterations in hydrodynamic diameter and polydispersity index (PDI) (Figure S1c, Supporting Information). We observed no significant changes in particle diameter and PDI after 24 h incubation in water and RPMI 1640 media. However, incubation in RPMI 1640 media (at 0 h and 24 h) resulted in an elevated PDI of the PS-Pd NPs compared to incubation in water. The increased PDI in RPMI 1640 media suggests a greater size distribution, potentially indicating agglomeration. However, considering the consistent hydrodynamic diameter and the relatively low PDI value (PDI of 0.23), we anticipate that the main size fraction of PS-Pd NPs remains unaltered in RPMI 1640 media.

2.2. PS-NPs Exert a Size-Dependent Impact on PBMC Viability and Functionality

Following human exposure, NPs could affect immune cells by triggering an inflammatory response, leading to chronic

A. Yilmazer
Department of Biomedical Engineering
Faculty of Engineering
Ankara University
Ankara 06100, Turkey
M. Orecchioni
Department of Pharmacology & Toxicology
Augusta University
Augusta 30912, United States
L. G. Delogu
Department of Biological Sciences
Khalifa University of Science & Technology
Abu Dhabi 127788, UAE

© 2024 The Author(s). Advanced Materials published by Wiley-VCH GmbH

15214095, 0, Downloaded from https://onlinelibrary.wiley.com/doi/10.1002/adma.202413413 by Ankara University Library, Wiley Online Library on [27/10/2024]. See the Terms and Conditions (https://onlinelibrary.wiley.com/terms-and-conditions) on Wiley Online Library for rules of use; OA articles are governed by the applicable Creative Commons License

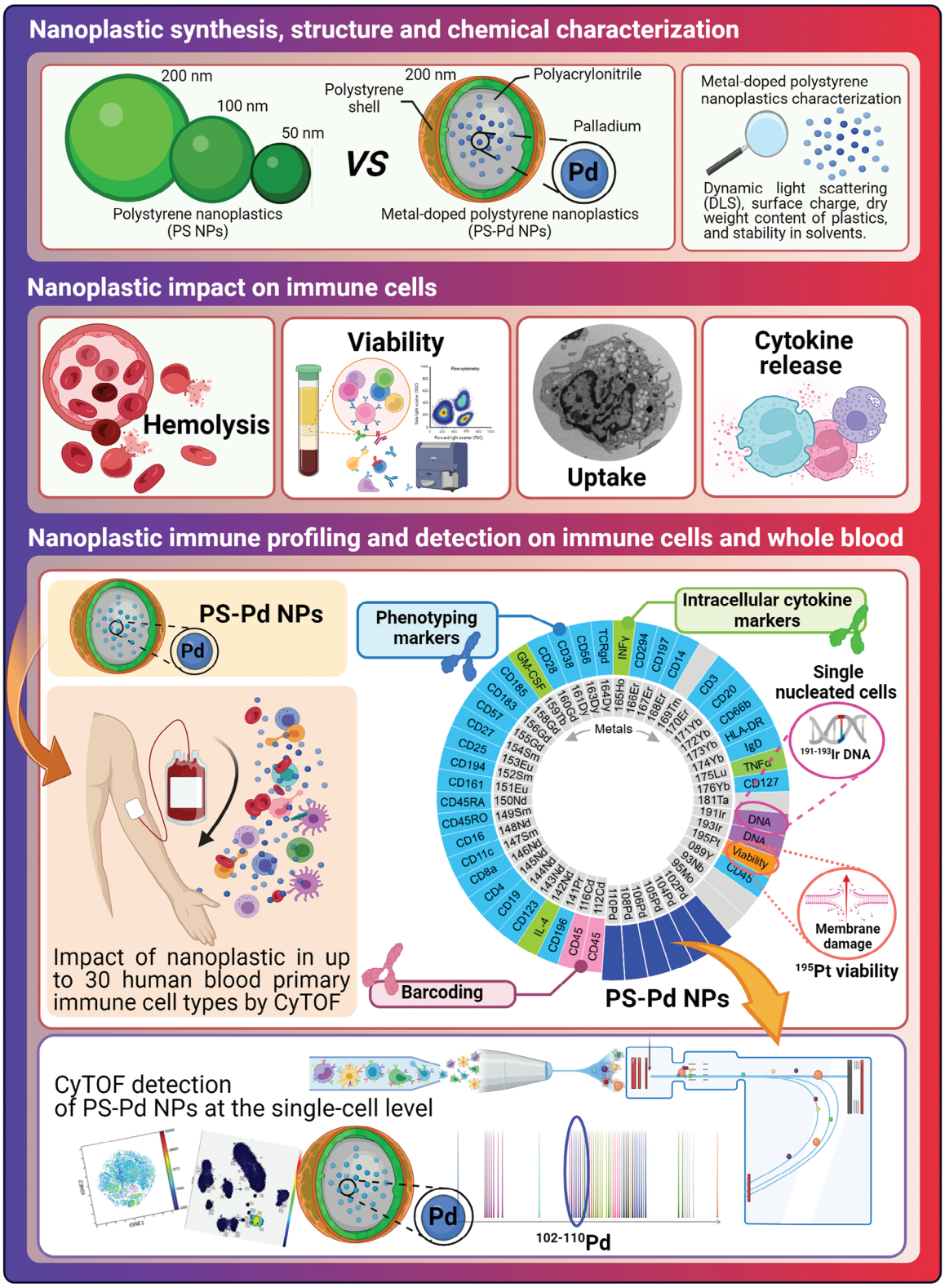


Figure 1. Workflow of the study. Study workflow showing the biological characterization of 50 to 200-nm polystyrene nanoplastics (PS NPs) and metal-doped polystyrene nanoplastics (PS-Pd NPs shell) on peripheral blood mononuclear cells and whole blood. We assessed NP impact on up to 30 human blood immune cell types by single-cell mass cytometry (CyTOF) ex vivo. Evaluation of cell viability, cell functionality, and NP uptake by CyTOF was performed.

© 2024 The Author(s). Advanced Materials published by Wiley-VCH GmbH

15214095, 0, Downloaded from https://onlinelibrary.wiley.com/doi/10.1002/adma.202413413 by Ankara University Library, Wiley Online Library on [27/10/2024]. See the Terms and Conditions (https://onlinelibrary.wiley.com/terms-and-conditions) on Wiley Online Library for rules of use; OA articles are governed by the applicable Creative Commons License

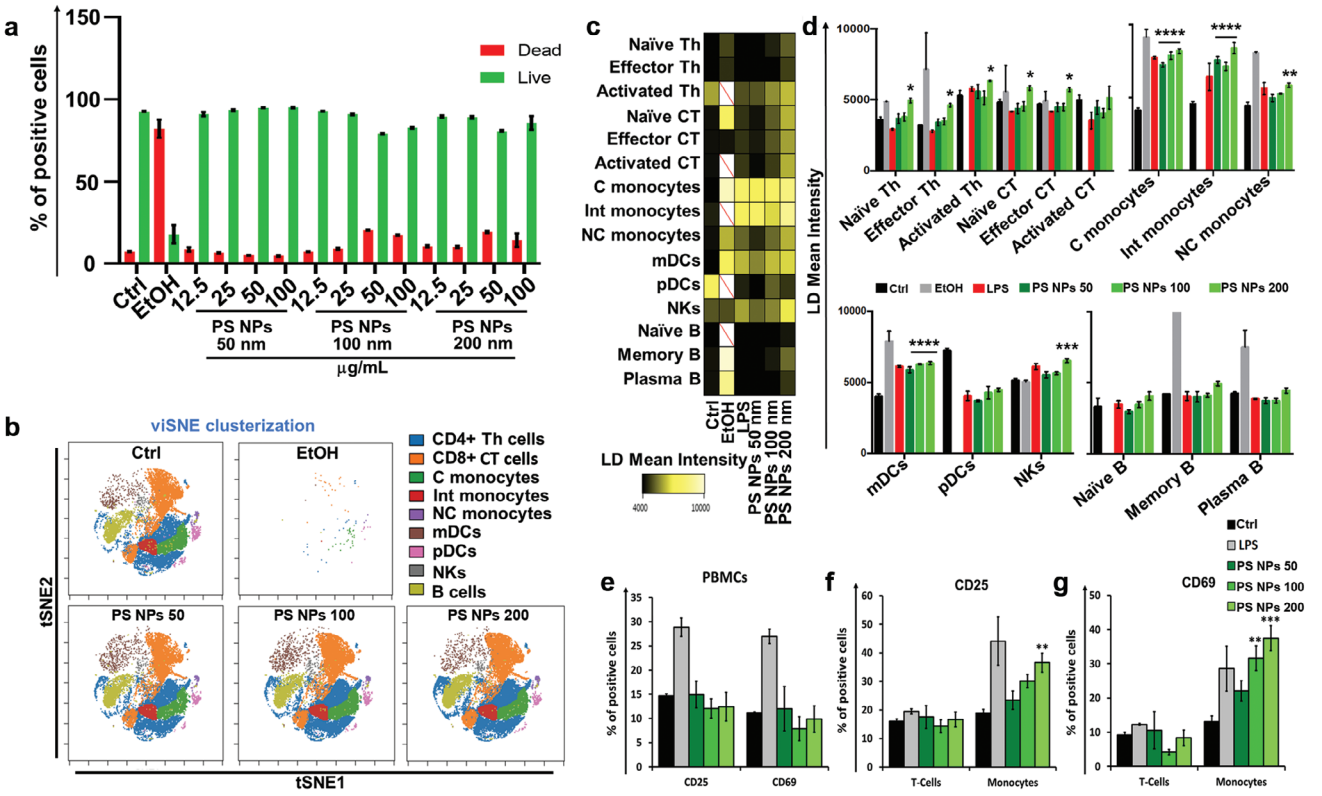


Figure 2. Cell viability and functional characterization of peripheral blood mononuclear cell subpopulations at the single-cell level. a) Cell viability staining analysis by flow cytometry and CyTOF. PBMCs were treated with 50–200 nm PS NPs (12.5, 25, 50, and 100 μg mL^{-1}) for 24 h or left untreated (Ctrl). EtOH 70% was used as a positive control to induce cell death. PBMCs were stained with Fixable Viability Staining 780. The histogram shows the percentage of positive live cells. b) The viSNE analysis clusterization reports the single-cell subpopulation identified from PBMCs. Immune cell cluster morphology plots after treatment with each NPL are reported. c) Heat map of LD mean marker expression ratio for all gated immune subpopulations. d) Histograms of cisplatin mean marker expression ratio for gated T cell, monocyte, dendritic cell, NK cell, and B cell subpopulations. e-g) Cell activation staining analysis by flow cytometry. Cells were treated with 50 μg mL^{-1} PS NPs 50 nm, PS NPs 100 nm, and PS NPs 200 nm for 24 h or left untreated (Ctrl). LPS (2 μg mL^{-1}) was used as a positive control. PBMCs were stained with CD25-PE and CD69-PE-Cy7, and cell activation was evaluated and expressed as a percentage of total cell number. e) Representative flow cytometric analysis for CD25-PE and CD69-PE-Cy7 staining in PBMCs. f,g) Cell activation is evaluated using CD25-PE staining in either T cells or monocytes and expressed as a percentage of the total cell number. Data are presented as the mean ± standard deviation (SD) of three independent samples. Statistical significance was determined using two-way ANOVA with Tukey's multiple comparison test between treated and untreated (Ctrl) groups. The significance levels are denoted as follows: *$p < 0.05$, **$p < 0.01$, ***$p < 0.001$, ****$p < 0.0001$. Heatmaps were generated on the concatenated files.

inflammation and immune dysregulation.[43] Additionally, NPs may interfere with immune cell activities such as phagocytosis and cytokine release,[59] compromising the ability of the immune system to fight pathogens. It has been demonstrated that NP size can play an important role in determining their toxic effects.[60,61] Therefore, we initially evaluated the biocompatibility of PS NPs with different sizes (50, 100, and 200 nm) on human immune cells ex vivo. Peripheral blood mononuclear cells (PBMCs) were treated with different concentrations (12.5–100 μg mL^{-1}) of PS NPs for 24 h. After incubation, we evaluated total PBMC apoptosis and necrosis by flow cytometry. Even at the highest concentration (100 μg mL^{-1}), no significant loss of cell viability was observed compared to the negative control, regardless of the particle size (**Figures** 2a and S2, Supporting Information).

To discern the effects of NPs on a wide variety of immune cell subpopulations, we selected the intermediate concentration of 50 μg mL^{-1}. We evaluated the impacts of PS NPs (50, 100, and 200 nm) by the CyTOF technology after treatment of PBMCs for 24 h. EtOH 70% was used as a positive control. First, we analyzed eleven clusters of differentiation markers (CDs) present on cell surfaces (i.e., CD3, CD4, CD8a, CD19, CD14, CD16, CD11c, CD123, CD45RA, CD27, and HLADR) to dissect fifteen significant CD45+ immune cell populations with their relative immune subsets: T helper cells (Th cells), naive Th, effector Th, memory Th, activated Th cells, cytotoxic T cells (CT cells), naive CT, effector CT, memory CT, activated CT cells, classical monocytes (C monocytes), intermediate monocytes (Int monocytes), non-classical monocytes (NC monocytes), natural killer cells (NK), B cells, B naive, B memory, plasma B cells, myeloid and plasmacytoid dendritic cells (mDCs and pDCs, respectively) (Figure 2b,c). Figure S3, Supporting Information shows the gating strategy used to identify all the 15 different immune cell subpopulations by CyTOF.

We assessed PBMC viability at the single-cell level using cisplatin (Cis) staining, which is based on the ability of Cis to enter late apoptotic and necrotic cells (Figure 2c,d). Overall, the largest

© 2024 The Author(s). Advanced Materials published by Wiley-VCH GmbH

15214095, 0, Downloaded from https://onlinelibrary.wiley.com/doi/10.1002/adma.202413413 by Ankara University Library, Wiley Online Library on [27/10/2024]. See the Terms and Conditions (https://onlinelibrary.wiley.com/terms-and-conditions) on Wiley Online Library for rules of use; OA articles are governed by the applicable Creative Commons License

NPs (i.e., 200-nm PS NPs) exerted higher toxicity on all the immune cell subtypes identified, suggesting a size-dependent effect on the ability of PS NPs to impair cell viability (Figure 2d). In particular, 200-nm PS NPs significantly decreased the cell viability of all monocyte and T cell subpopulations except for activated CT cells. In addition, a similar impact was observed on mDCs and NKs (Figure 2d). On the other hand, the effect of PS NPs with smaller sizes (i.e., 50 and 100 nm) was limited to C. monocytes, Int. monocytes, and mDCs, inducing a reduction of this subpopulation viability similar to the largest PS NPs. The increased toxicity toward monocytes and DCs observed for all the PS NPs, regardless of their size, may be due to the higher phagocytic activity of these cell types.[62] Intriguingly, no significant decrease in cell viability was observed in B cell subpopulations.

These findings demonstrate size-dependent NP-induced cytotoxicity specific for a broad range of distinct immune cell subpopulations. A similar correlation between the size and toxicity of nanoparticles has been documented for immune cells[63] as well as other types of cells, such as human alveolar basal epithelial cells (A549),[60] human umbilical vein endothelial cells (HUVECs),[61] and gastric cells (SNU-1).[59]

Next, we investigated the impact of NPs on the functionality of PBMCs by monitoring different immune activation parameters (Figure 2e–g) and cytokines (Figures S4 and S5, Supporting Information). To evaluate PBMC activation, we analyzed CD69 (C-Type lectin protein) and CD25 (α-chain of the IL-2 receptor), respectively, early and late activation markers. To this end, we incubated PBMCs with 50 μg mL^{-1} of PS NPs (50, 100, and 200 nm) for 24 h and analyzed the cells by flow cytometry. We observed no significant changes in the selected markers induced by PS NPs in total PBMCs and T cells (Figure 2e–g). On the contrary, the particles induced a significant size-dependent increase in CD25^{+} and CD69^{+} monocytes (Figure 2f), indicating an immune response slightly biased toward the activation as previously reported for other PS-NPs.[64] To contextualize the pro-inflammatory status, we evaluated the production of cytokines at the single-cell level by CyTOF after treatment with 50 μg mL^{-1} of PS NPs (50, 100, and 200 nm) for 24 h. To minimize protein transport inhibitor-mediated toxicity, they were added 6 h before the end of the incubation, allowing the profiling of late-stage regulated cytokines at the single-cell level (Figures S4 and S5, Supporting Information). In these settings, we observed signs of T cell-mediated inflammation with a significant increase of IL-4 and TNF-α in activated CT cells and HLA-DR in activated Th cells after exposure to 200-nm PS NPs (**$p < 0.01$). A slight increase in IL-4 production was observed in activated Th cells also after the exposure to 50-nm PS NPs as well as GrB and perforin in NC monocytes (*$p < 0.1$).

In Int. monocytes, together with the increase of IL-4 and IL-5, the 200-nm PS NPs induced a slight but significant change in the production of pro-inflammatory IL-6, in agreement with previously reported data.[27,64] In addition, the largest PS NPs increased TNF-α in Plasma B cells, an effect compatible with a response against external agents.[65]

Overall, our data demonstrate that larger PS NPs (200 nm) are more effective in inducing cytokine production and immune cell activation, suggesting a role of particle size in their ability to affect immune cell functions, in particular in T cells and monocytes. The larger the NP, the greater the surface area, which may be conducive to increased cytokine production, suggesting that size is a critical factor in their immune impact.[66] Similarly, functionalization is known to play a significant role in modulating the response of immune cells after incubation with PS NPs. We investigated these factors by assessing cell viability and activation in established cell lines, Jurkat and THP-1, after 24-h incubation with PS NPs of different sizes and functionalization (200 nm COOH, 500 nm COOH, and 500 nm NH) at a concentration of 50 μg mL^{-1}. After 24h of incubation, larger PS NPs (500 nm COOH and 500 nm NH) at a dose of 50μg mL^{-1} significantly affected cell activation, as evidenced by changes in CD69 marker expression (Figure S6, Supporting Information). Notably, these effects were not related to the different chemistries of the PS NPs (COOH and NH), as aminated surface modifications did not show significant differences in our assays. This lack of impact from chemical modifications may be due to the formation of a protein corona around the NPs, which can mask the effects of polymer chemistry.[67] The significant activation observed in both cell lines, indicated by increased CD69 expression, demonstrates that the larger PS NPs trigger a stronger immune response without compromising cell survival. Our data align with previous studies on other immune cell types showing an impact of NP size on the modulation of inflammatory mediators. For instance, Prietl *et al.* observed that in human macrophage-like cells exposed to 20–1000-nm PS nanospheres, only larger particles (500- and 1,000-nm size) enhanced the secretion of IL-6.[27] Similarly, in Rothen-Rutishauser *et al.*, 1,000-nm but not 78-nm PS spheres increased TNF concentrations in epithelial cells, macrophages, and DCs.[68]

To further explore the observed cytotoxic effects, we compared the impact of PS-Pd NPs and PS-NPs with similar size (200 nm) on total PBMC viability (Figure S7a, Supporting Information). The particle size was selected to ensure compatibility with potential NP cell uptake, as previously shown,[51] which is critical for accurately assessing their cytotoxic effects on immune cells.[69–71] Larger particles might be less efficiently internalized by cells, potentially affecting the reliability and significance of results. We treated PBMCs with 50 μg mL^{-1} of NPs for 24 h and analyzed the samples by flow cytometry. Similar to PS-NPs, PS-Pd NPs induced no significant effects on cell viability in total PBMCs. Even after gating monocytes and T cells, the NPs did not significantly impair cell viability (Figure S7b,c, Supporting Information).

To evaluate the potential hemolytic activity of NPs, human red blood cells were exposed to 50 μg mL^{-1} of PS NPs or PS-Pd NPs for 1 and 24 h (Figure S7d, Supporting Information). PS-Pd NPs induced hemolysis only after 24 h, while we observed no significant release of hemoglobin caused by PS NPs. Our data are in agreement with previous data analyzing 100-nm PS NPs (100 μg mL^{-1}) at the same incubation time,[72] while a concentration-dependent hemolytic activity for 50-nm PS NPs was reported at higher concentrations (500–2000 μg mL^{-1}).[73]

Then, we deepened our study by evaluating the uptake by transmission electron microscopy (TEM). As observed in Figure S8, Supporting Information, PBMCs were able to internalize both PS NPs and PS-Pd NPs after incubation with 50 μg mL^{-1} for 24 h. The particles did not compromise cell integrity, and no autophagy or cell death was observed in agreement with data obtained with other immune cells.[62] Our analysis further indicates that these NPs are predominantly localized within large vesicles and do not directly affect cellular organelles. NPs are known to modulate cellular oxidative stress, activating the immune

© 2024 The Author(s). Advanced Materials published by Wiley-VCH GmbH

RIGHTSLINK

15214095, 0, Downloaded from https://onlinelibrary.wiley.com/doi/10.1002/adma.202413413 by Ankara University Library, Wiley Online Library on [27/10/2024]. See the Terms and Conditions (https://onlinelibrary.wiley.com/terms-and-conditions) on Wiley Online Library for rules of use; OA articles are governed by the applicable Creative Commons License

response and leading to immunotoxicity.[74] To evaluate this aspect, we treated Jurkat and THP-1 with 50 μg mL^{-1} of PS NP for 24 h and measured reactive oxygen species (ROS) using the CellRox Green Flow Cytometry Assay. Our results showed a significant increase in ROS production in treated THP-1 and Jurkat cells (50% and 60%, respectively) compared to untreated cells, as indicated by the CellRox Green intensity assay (Figure S9, Supporting Information).

Since monocytes are the cells most affected by PS NPs incubation, we aimed to characterize the PS NP function at the molecular level. We performed bulk RNA sequencing and proteomic analysis on a monocytic cell line (THP1) following treatment with 50 μg mL^{-1} of PS NP for 24 h. After treatment, RNA and proteins were extracted for subsequent RNA sequencing and proteomic profiling. Volcano plots provided a clear visualization of significant changes in gene expression and protein production (**Figure 3**a,b). Specifically, transcriptome analysis revealed that 259 genes were downregulated (Fold Change >-0.25, blue, *p*-value <0.05) and 297 genes were upregulated (Fold Change <0.25, red, *p*-value <0.05) (Figure 3a), while proteome analysis identified 41 proteins as downregulated and 31 as upregulated (Figure 3b) as reported in Table S1, Supporting Information. These molecules represent potential biomarkers that could elucidate the mechanisms underlying cellular responses to PS NP treatment. Several genes and proteins associated with oxidative stress were identified in both the transcriptome and proteome datasets. From the transcriptome analysis, genes such as *GSR* (Glutathione-Disulfide Reductase), *G6PD* (Glucose-6-phosphate dehydrogenase), and *PRDX4* (Peroxiredoxin 4) were significantly upregulated.[75–77] These genes play crucial roles in mitigating oxidative stress by catalyzing the reduction of glutathione disulfide to glutathione (*GSR*), a major cellular antioxidant, reducing peroxides (*PRDX4*), and providing substrates to prevent oxidative damage (*G6PD*). In the proteome analysis, we found proteins like ALDH2 (Aldehyde Dehydrogenase 2) and PRDX1 (Peroxiredoxin 1). These proteins are involved in maintaining cellular redox balance, reducing oxidative damage, and detoxifying harmful compounds.[78–80] The upregulation of these oxidative stress-related genes and proteins suggests an adaptive response by the cells to counteract increased oxidative stress induced by the PS NP treatment. To this extent, the modulation of several ribosomal genes and proteins also suggests increased cell stress and possibly cell death.[81] This aligns with existing literature where treatments that induce oxidative stress have been shown to upregulate similar protective genes and proteins.[82] Intriguingly, among the top upregulated pathways identified by gene expression analysis, we found the AIM2 inflammasome pathway (Figure 3c). The AIM2 inflammasome is responsible for sensing self and non-self DNA in the cytosol. This detection initiates inflammasome assembly and IL-1β release, promoting inflammation.[83] Together with the previous ROS data, this suggests that PS NP may induce damage to the mitochondria, leading to DNA release and inflammasome activation. At the same time, we found the downregulation of TNFR1-mediated ceramide production and IL-38 signaling, indicating suppression of anti-inflammatory mechanisms, potentially leading to an overall increase in inflammation and cytokine production.[84,85] The upregulation of the SMAC-XIAP-regulated apoptotic response pathway suggests an increase in mediated cell death, as SMAC (Second Mitochondria-derived Activator of Caspases) promotes apoptosis by inhibiting XIAP (X-linked Inhibitor of Apoptosis Protein), thereby facilitating caspase activation which is also needed for the inflammasome pathway activation.[86] Similarly, the modulation of the RUNX1 in the differentiation of myeloid cells pathway is known to promote inflammation and an improper monocyte maturation that may lead to Acute Myeloid Leukemia (AML).[87] The proteomic analysis confirmed the regulation of similar pathways, including the RUNX1-regulated transcription of genes involved in the interleukin signaling pathway (Figure 3d). The upregulation of apoptosome activity is a crucial complex in the intrinsic apoptosis pathway.[87] The upregulation of pathways associated with defective HEXA (HEXA gene mutations leading to Tay-Sachs disease) causing GM2 gangliosidosis also implies increased cellular stress.[88] Conversely, the downregulation of the Nonsense-Mediated Decay (NMD) pathway, which usually degrades faulty mRNA transcripts, may result in the accumulation of defective proteins, contributing to cellular stress and apoptosis.[89] Finally, the modulation of amine oxidation pathways and aldehyde generation, such as monoamine oxidases, MAOA, and MAOB, further highlights that PS NPs induced apoptosis and ROS formation through enhanced cellular stress mechanisms (Figure 3d). These data collectively suggest that PS NPs significantly impact monocytes by inducing mitochondrial damage, triggering inflammasome activation, promoting apoptosis, and enhancing cellular stress, leading to a complex pro-inflammatory response.

2.3. PS-Pd NPs Can be Detected and Quantified by CyTOF at the Single-Cell Level in 30 Immune Cell Subpopulations

Overcoming the limitation of fluorescently labeled NPs, we explored the potential trackability of PS-Pd NPs, which are measurable by CyTOF, to study the interactions of NPs with the immune cells. The specific atomic mass of Pd enabled the mass spectrometry detection of PS-Pd NPs in the relevant channels ($^{102–110}$Pd). The mass spectra of PS-Pd NPs and the dynamic range of $^{102–110}$Pd were determined by CyTOF solution mode (**Figure 4**a,b). An NP concentration ranging from 0.0076 to 50 μg mL^{-1}) was tested. $^{102–110}$Pd peaks were compared to standard heavy metal mass spectra (Ce, Eu, Ho, and Lu) reported in Figure 4a as controls. The ^{108}Pd peak was chosen for the following measurements as it was the most intense and easily identifiable m/z ratio among all the $^{102–110}$Pd peaks. The dynamic range of quantification of PS-Pd NPs was linear up to a particle concentration of 50 μg mL^{-1}, and Pd was detectable by mass cytometry across the entire concentration range (0.0076–50 μg mL^{-1}) (Figure 4b).

We performed a quantitative evaluation of the presence of Pd at the single-cell level. To this end, we treated PBMCs with 50 μg mL^{-1} of PS-Pd NPs for 24 h. The intermediated sub-cytotoxic concentration of 50 μg mL^{-1} and the 24 h time point were selected based on the results obtained by flow cytometry (Figure S10a, Supporting Information) and to avoid the saturation of Pd intensity on the CyTOF platform while still ensuring noticeable changes in cellular signaling. The same concentration was also found to modulate monocyte activation, as indicated by CD25

© 2024 The Author(s). Advanced Materials published by Wiley-VCH GmbH

15214095, 0, Downloaded from https://onlinelibrary.wiley.com/doi/10.1002/adma.202413413 by Ankara University Library, Wiley Online Library on [27/10/2024]. See the Terms and Conditions (https://onlinelibrary.wiley.com/terms-and-conditions) on Wiley Online Library for rules of use; OA articles are governed by the applicable Creative Commons License

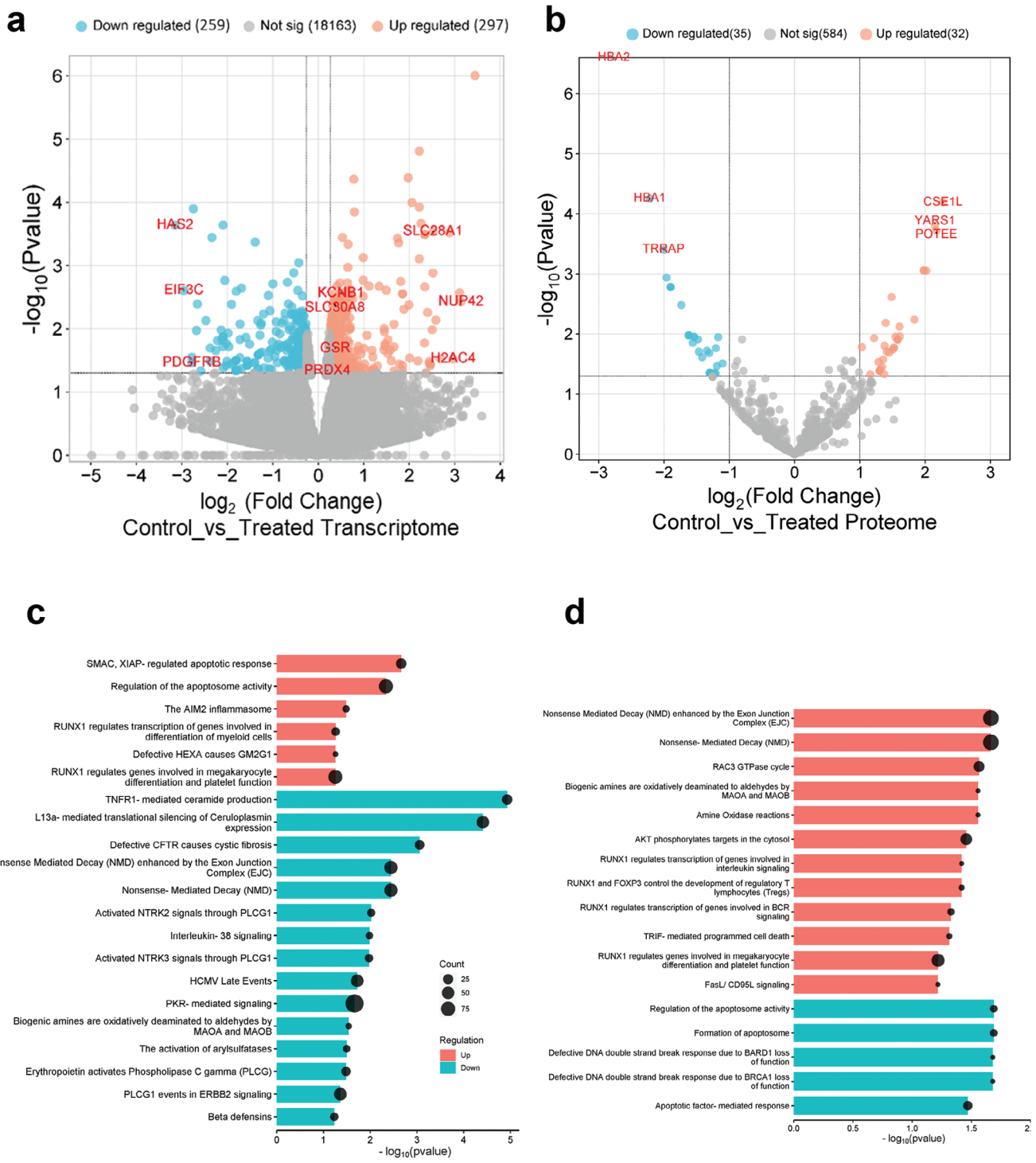


Figure 3. Transcriptomic and Proteomic Functional Profiling of PS-NP in a Monocytic Cell Line. THP1 cells were seeded in a 24-well plate at a density of 2×10^6 cells per well and treated with PS-NP (50 μg mL^{-1}) for 24 h. a,b) Volcano plots showing differently expressed (a) genes and (b) proteins, with an FDR < 0.05 following PS-NP treatment. c,d) Pathway analysis using ReactomePA reporting significantly modulated pathways with a log10 p value < 1.3 for differentially expressed (c) genes and (d) proteins in PS-NP treated cells. Predicted upregulated (red) and downregulated (light-blue) pathways are reported.

© 2024 The Author(s). Advanced Materials published by Wiley-VCH GmbH

15214095, 0, Downloaded from https://onlinelibrary.wiley.com/doi/10.1002/adma.202413413 by Ankara University Library, Wiley Online Library on [27/10/2024]. See the Terms and Conditions (https://onlinelibrary.wiley.com/terms-and-conditions) on Wiley Online Library for rules of use; OA articles are governed by the applicable Creative Commons License

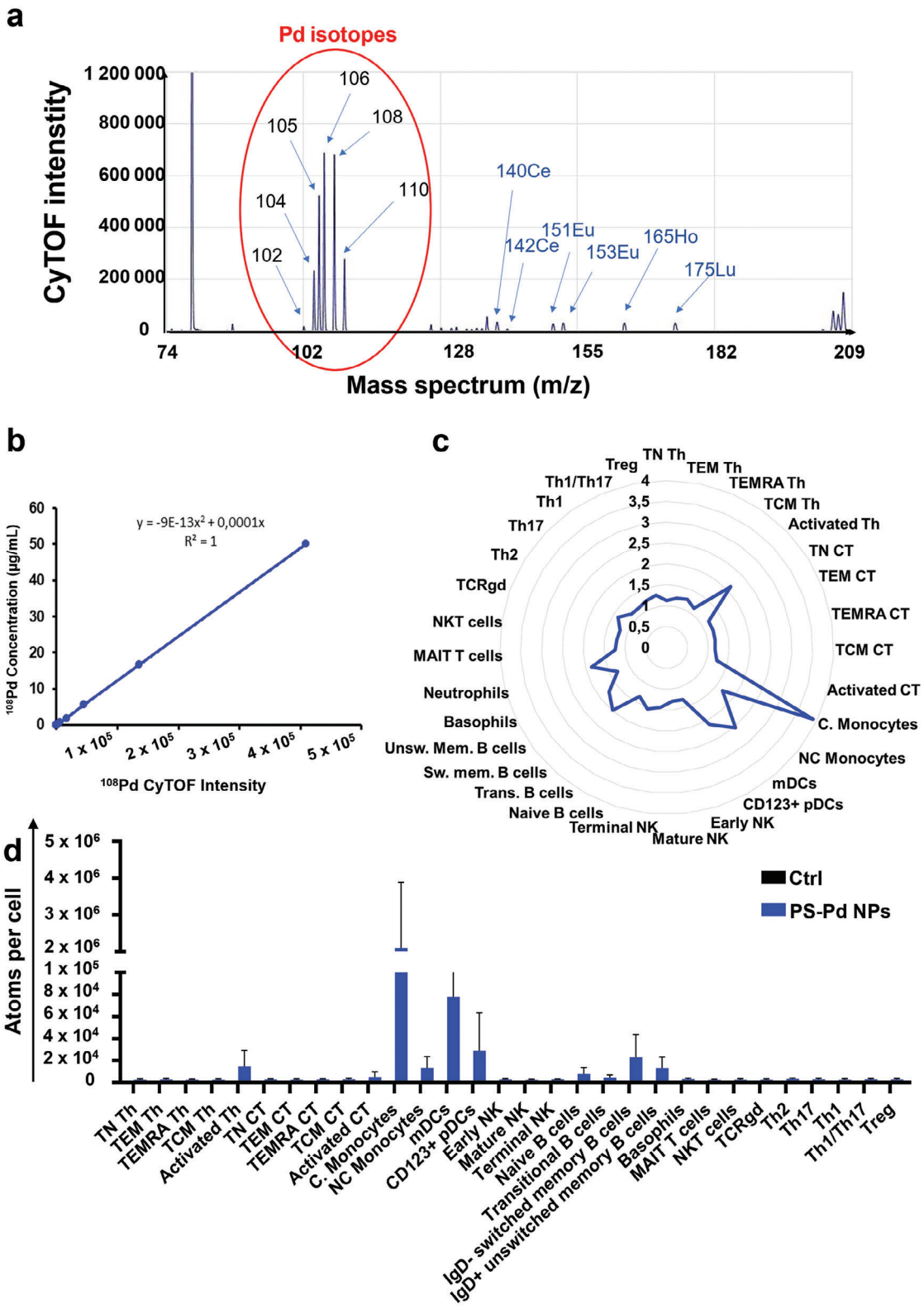


Figure 4. Palladium quantification determined by CyTOF. a) The mass spectrum of PS-Pd NPs determined by CyTOF solution mode and lanthanide element calibration beads were applied as controls. b) Dynamic range of ^{108}Pd determined by CyTOF solution mode. c) Radar chart reporting the number of ^{108}Pd atoms per cell in all PBMC subpopulations. d) Number of ^{108}Pd atoms per cell determined from direct atom analysis in all PBMC subpopulations after the 24-h treatment of PBMCs (50 µg mL^{-1} each).

© 2024 The Author(s). Advanced Materials published by Wiley-VCH GmbH

15214095, 0, Downloaded from https://onlinelibrary.wiley.com/doi/10.1002/adma.202413413 by Ankara University Library, Wiley Online Library on [27/10/2024]. See the Terms and Conditions (https://onlinelibrary.wiley.com/terms-and-conditions) on Wiley Online Library for rules of use; OA articles are governed by the applicable Creative Commons License

expression, without affecting cell viability (Figure S10b, Supporting Information).

The calibration of the TOF detector (see Section 4.8) using a calibration curve of Pd standards (0–50 μg mL^{-1}) (Figure 4b) enabled the direct enumeration of Pd ions and, thereby, the mean number of atoms accumulated per cell (Figure 4c,d). PS-Pd NPs were detectable by mass cytometry in all the 30 immune subpopulations analyzed, already starting from the lowest concentration used (0.0076 μg mL^{-1}) (Figure 4c,d). In particular, the number of Pd atoms per cell reported the highest signal in the C monocyte subpopulation, followed by mDCs, pDCs, memory B cells, and activated Th.

2.4. PS-Pd NPs are Trackable in Immune Cells after Contamination of Human Blood, Allowing for the Simultaneous Immune Screening on 30 Immune Cell Subpopulations by CyTOF

To reveal the potential for plastic particles to exert toxic effects, interfere, and eventually be internalized from the immune cells present in the bloodstream after blood contamination, whole human blood was treated with different concentrations (10–500 μg mL^{-1}) of PS-Pd NPs for 24 h and analyzed using CyTOF. The selection of Pd as a metal label ensured the compatibility of PS-Pd NPs with the commercial (metal-tagged) antibody panels for CyTOF immunophenotyping (Table S2, Supporting Information), avoiding the overlap of the

The impact of PS-Pd NPs on cell viability was evaluated at the single-cell level on 30 immune cell subpopulations. From human whole blood, 30 distinct immune cell subtypes were identified according to the expression profile of several clusters of differentiation (CD) markers on the cell surface (Figure S11, Supporting Information). The live cell membrane-impermeable dye Cell-ID Intercalator-103Rh, a cationic nucleic acid intercalator that contains natural-abundance rhodium (103Rh), was used in CyTOF analysis for discrimination of dead cells from live cells.

As shown in **Figure 5**a,b, blood exposure to 500 μg mL^{-1} of PS-Pd NPs induced a significant decrease in cell viability in C. Monocytes and Int. Monocytes. All identified major immune subpopulations in treated and untreated samples are also reported as percentages of live cells in the high-dimensional Cen-se′ maps, a high-resolution and highly parallelized variant of the t-SNE algorithm (Figure S12a, Supporting Information), and as gemstone representation (Figure S12b, Supporting Information). A slight but non-significant change in the distribution of the subpopulation percentage among live cells was observed mainly at the highest concentration tested (500 μg mL^{-1}) (Figure S12c,d, Supporting Information).

In addition, the Pd signal was exploited to evaluate the internalization of plastic particles in immune cells after blood exposure. The differential uptake of PS-Pd NPs was analyzed by CyTOF in a wide range of PBMC subtypes after exposure of human whole blood to different concentrations (10–500 μg mL^{-1}) of PS-Pd NPs for 24 h. As shown in Figure 5c,d, PS-Pd NPs were successfully detected at the single-cell level, revealing their interactions with all the immune cell subpopulations identified. In particular, a statistically significant concentration-dependent uptake was observed in all the subtypes of monocytes (starting from 50 μg mL^{-1} in Int. monocytes and NC monocytes, and already from 10 μg mL^{-1} in C. monocytes) and B cells (starting from 100 μg mL^{-1} in naïve and memory B cells, and 50 μg mL^{-1} in plasma B cells). Interestingly, at the highest concentration tested (500 μg mL^{-1}), all the immune cell subsets could significantly internalize PS-Pd NPs from contaminated blood. We also evaluated the distribution of ^{108}Pd in all the immune subpopulations by computational Cen-se' (Figure S13a, Supporting Information) at different concentrations (10–500 μg mL^{-1}). At 500 μg mL^{-1}, ^{108}Pd was visibly present in monocytes and mDCs. Similarly, by performing an in-depth gating on Pd+ immune cell subpopulations (Figure S13b, Supporting Information), C monocytes (72.1%) followed by Int monocytes (2.2%) were the central immune subsets able to internalize PS-Pd NPs (Figure S13b,c, Supporting Information). The 50 μg mL^{-1} concentration was compared with the 500 μg mL^{-1} concentration in isolated PBMCs (Figure S14, Supporting Information). No differences were found in population distribution (Figure S14a, Supporting Information) and viability (Figure S14b, Supporting Information). As expected, the NP uptake was higher for the 500 μg mL^{-1} concentration (Figure S14c, Supporting Information). The signal of PS-Pd NP was higher in monocyte subpopulations for both concentrations.

Subsequently, we investigated the possible correlation between NP uptake and impacts on monocyte and eosinophils cell viability, as they represented the main populations affected by the exposure of human blood to NPs (Figure 5e). As shown in the bar graph reporting the percentage of live and dead cells and the relative positivity or negativity to Pd^{108}, the increase in NPs association was associated with a decrease in cell viability in all monocyte subpopulations. Interestingly, only a small percentage of dead cells did not become associated with NPs, suggesting that association plays a central role in their toxic effects.

Together with the immunophenotyping, to simultaneously evaluate the inflammogenic activity of PS-Pd NPs, four major inflammatory cytokines (interleukin 4 (IL-4), interferon-gamma (IFN-γ), tumor necrosis factor (TNF-α) and granulocyte-macrophage colony-stimulating factor (GM-CSF)) were analyzed across 30 immune cell subpopulations. Based on the percentage of positive cells to the cytokines displayed for each immune subpopulation as histograms (**Figure 6**a,b) and heatmaps (Figure 6c), PS-Pd NPs induced a pro-inflammatory activity. The results show the overall immunostimulatory effect of PS-Pd NPs in all cell subsets (Figure 6a–c**)**. The percentage of positive cells to TNF-α and IFN-γ was higher in T helper, B cells, NK, and DC cells as well as to IL4 and GM-CSF proteins also in all the T cell populations, mediating together the immune activation after exposure to pro-inflammatory stimuli in many immune cell populations.[90,91] Similar behavior was reported in the literature for PS NPs of larger sizes and higher concentrations in PBMCs[32] and skin cells,[92] suggesting that the PS NP stimulus is pro-inflammatory.[93]

2.5. Biodistribution of PS-Pd NPs in Mice: In Vivo Accumulation in Spleen and Liver with High Internalization by Monocytes and Dendritic Cells

We then investigated the in vivo biodistribution and impact of PS-Pd NPs in mice at the tissue and single-cell level by CyTOF. PS-Pd NPs were injected I.V. into C57BL/6J male mice at a dose

© 2024 The Author(s). Advanced Materials published by Wiley-VCH GmbH

RIGHTSLINK
15214095, 0, Downloaded from https://onlinelibrary.wiley.com/doi/10.1002/adma.202413413 by Ankara University Library, Wiley Online Library on [27/10/2024]. See the Terms and Conditions (https://onlinelibrary.wiley.com/terms-and-conditions) on Wiley Online Library for rules of use; OA articles are governed by the applicable Creative Commons License

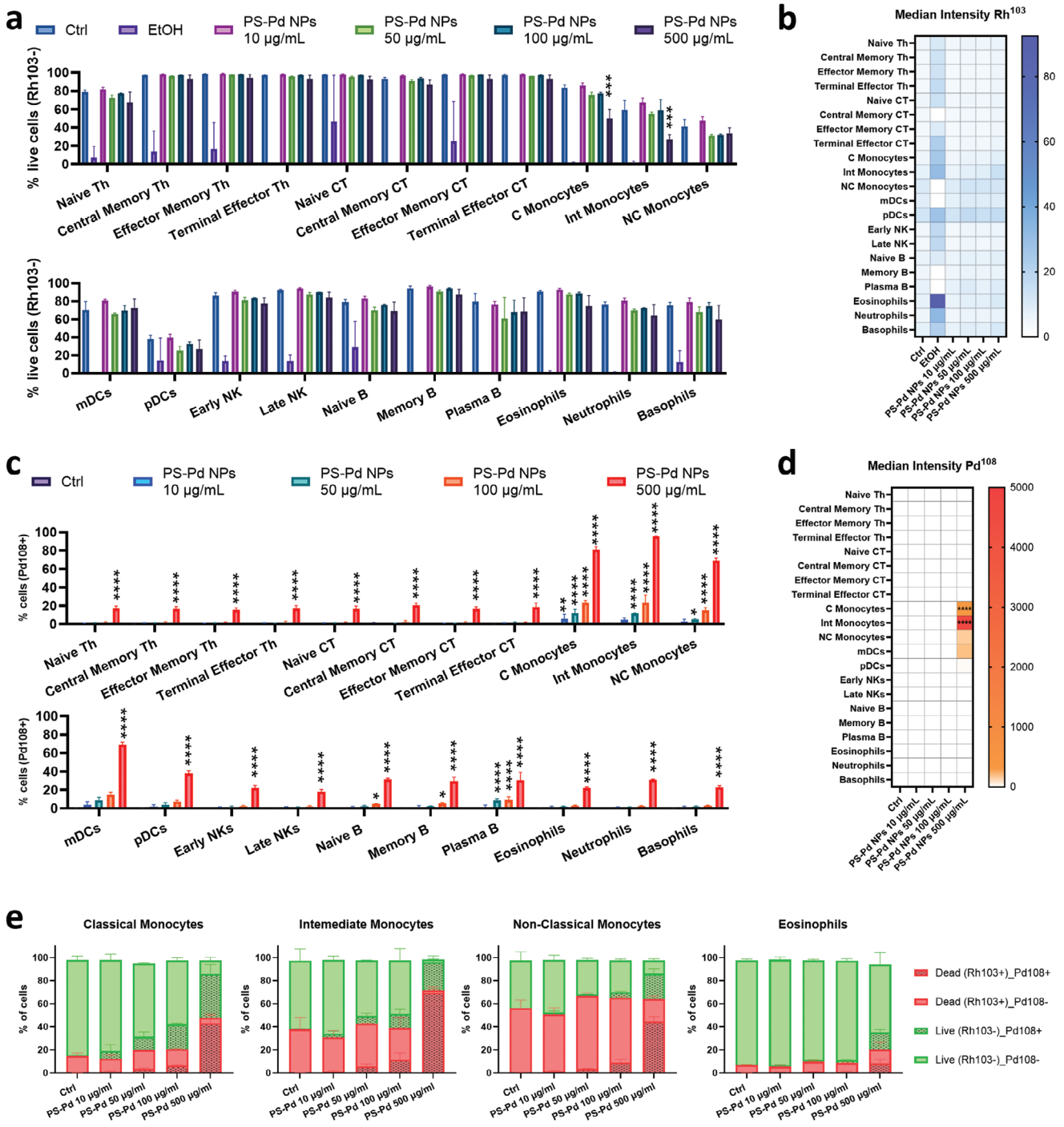


Figure 5. Impact of PS-Pd NPs on immune cells and correlation between viability and uptake. Human whole blood was treated with 10–500 µg mL^{-1} of PS-Pd NPs for 24 h or left untreated in 21 distinct immune cell subpopulations (Ctrl). a) Bar graph reporting the different distribution % of live cells (Rh103-) and b) Heatmap reporting the different distribution of the Median Intensity Rh^{103} c) Bar graph reporting the different distribution % of cells (Pd108+) and d) Heatmap reporting the different distribution of the Median Intensity Pd^{108} e) Bar graph showing the percentage of live and dead cells and the relative positivity or negativity to Pd^{108}. Data are presented as mean ± ST.D. of three independent samples. *$p < 0.05$; ** $p < 0.01$; *** $p < 0.001$; **** $p < 0.0001$, by two-way ANOVA Tukey's multiple comparison test between untreated (Ctrl) and treated samples.

© 2024 The Author(s). Advanced Materials published by Wiley-VCH GmbH

RIGHTSLINK

15214095, 0, Downloaded from https://onlinelibrary.wiley.com/doi/10.1002/adma.202413413 by Ankara University Library, Wiley Online Library on [27/10/2024]. See the Terms and Conditions (https://onlinelibrary.wiley.com/terms-and-conditions) on Wiley Online Library for rules of use; OA articles are governed by the applicable Creative Commons License

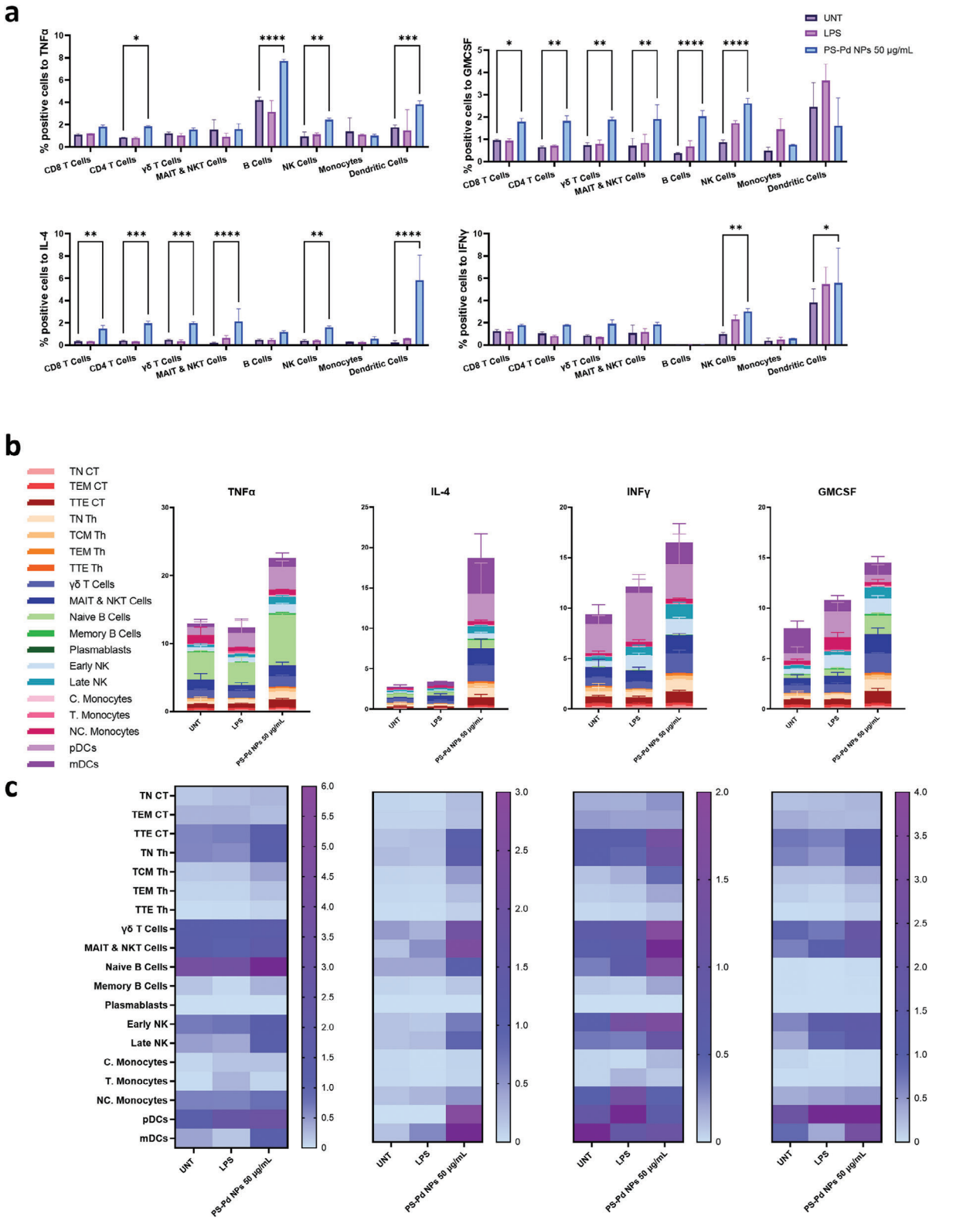


Figure 6. Single-cell cytokine analysis on 19 blood immune cells subpopulations. a,b) Histograms, and c) Heatmaps showing geometrical mean marker intensity of IL4, INFy, TNFα, GM-CSF for gated immune cell subpopulations after treatment of PBMCs with 50 µg mL^{-1} of PS-Pd NPs for 24 h. Upregulated (violet squares) or downregulated (light-blue squares) proteins are indicated. Data are presented as mean ± ST.D. of three independent samples. *p < 0.05; **p < 0.01; ***p < 0.001; ****p < 0.0001, by two-way ANOVA Tukey's multiple comparison test.

© 2024 The Author(s). Advanced Materials published by Wiley-VCH GmbH

RIGHTSLINK

15214095, 0, Downloaded from https://onlinelibrary.wiley.com/doi/10.1002/adma.202413413 by Ankara University Library, Wiley Online Library on [27/10/2024]. See the Terms and Conditions (https://onlinelibrary.wiley.com/terms-and-conditions) on Wiley Online Library for rules of use; OA articles are governed by the applicable Creative Commons License

of 10 μg g^{-1}. After 24 h, mice were euthanized, and tissues were harvested and processed to obtain a single-cell suspension that was stained with an antibody cocktail and analyzed by CyTOF. We studied PS-Pd NP effects on cell viability and uptake in major immune cell subpopulations from the blood, liver, and spleen of mice (n = 3 per group).

We observed a significant increase in dead cells (195Pt+) in conventional dendritic cells (cDC) and macrophages in the liver and cDC in the spleen (**Figure** 7a). This indicates that PS-Pd NPs accumulation is toxic in these populations.

Furthermore, analysis of Pd108 median intensity revealed substantial PS-Pd NP uptake in liver cDCs and macrophages (Figure 7b). These findings were further supported by pacMAP visualization[85] (Figure 7c) and bar graph analysis (Figure 7d), which showed higher accumulation and immune cell uptake in the liver compared to blood and spleen. Several other immune cells, including T cells and B cells, showed internalization of PS-Pd NPs, particularly in the liver, where 20% of CD4+ and CD8+ T cells, B cells, and NK cells, and 30% of monocytes and granulocytes were positive for Pd108 signal (Figure 7d).

Several authors have previously reported that nanoparticles' size, composition, and surface characteristics dictate their biodistribution profile and stability within the body. It has been well-documented that larger particles tend to accumulate more in the liver compared to smaller ones.[71,94–96] This is one of the first reports demonstrating the in vivo accumulation of PS-NPs and their interaction with the immune system in the liver, spleen, and blood. This accumulation is largely attributed to monocytes, macrophages, and DCs in these tissues, which are known to capture circulating particulates and nano/macromolecules.

3. Conclusions

In conclusion, our data underlines the advantage of using high-dimensional approaches such as CyTOF to study the effect of plastics on human health. In this direction, CyTOF was able to reveal the different size-dependent impacts and biodistribution of a selection of model NPs on the complexity of the pool of immune cell subpopulations, which is not appreciable by the canonical flow cytometry technique. Regarding NPs cytotoxicity evaluation, these results emphasize the urgency and importance of focusing on human blood and immune toxicological research using primary human blood immune cells (e.g., PBMCs), in addition to immortalized models.

Moreover, we presented evidence that NPs can interact, interfere, and translocate into the immune cells in the bloodstream after blood exposure by utilizing Pd-doped NPs, which are readily detectible by CyTOF and compatible with commercial metal-tagged antibodies. This study demonstrates PS-Pd NP detection at the single-cell level in human whole blood and primary immune cells. To this end, we used the $^{102–110}$Pd channels to detect the PS-Pd NPs and simultaneously evaluated their impact across 30 primary human blood immune cell subpopulations. We successfully detected PS-Pd NPs across each cell subset, assessing their effects through high-dimensional immune profiling by CyTOF combined with other techniques, including TEM and flow cytometry. The assessment of the immune impact of PS-Pd NPs in terms of immune activation and cytokine production was possible with the CyTOF functional profiling. PS-Pd NPs increased the production of pro-inflammatory cytokines (IL-4, IFN-γ, TNF-α, and GM-CSF) in all the major populations analyzed.

The possibility of detecting and quantifying PS-Pd NPs by CyTOF at the single-cell levels and in multiple immune cell subpopulations while exploring their biological impact and tracking is expected to advance the toxicological assessment of NPs. By avoiding the limits of conventional labeling techniques, this work provides valuable insights into the potential health impact of NPs and serves as a proof of concept for studying the overall environmental and health implications of plastic pollution.

4. Experimental Section

Characterization of PS NPs and PS-Pd NPs: Monodisperse carboxylate polystyrene microspheres (PS NPs) (2.5% solids in water) of different sizes 50, 100, and 200 nm were purchased from Polysciences Europe Gmbh. PS-Pd NPs were synthesized in-house as previously published[46] and characterized in terms of size, surface charge, and plastic content in solution. The size and zeta potential of the PS-Pd NPs were measured by DLS and zeta potential, respectively, with the Zetasizer Nano ZS (Malvern) (Figure S1a, Supporting Information). All initial characterization measurements were performed in dd-H2O at room temperature.

To prepare PS-Pd NPs for Scanning Electron Microscopy (SEM) image analysis (Figure S1b, Supporting Information), an aqueous suspension of particles was deposited on a carbon stick and allowed to dry overnight in a clean environment coated with a Pd/Pt 4 nm layer prior to analysis. Images were acquired using a Hitachi SU5000 operating at 5.0kV at a working distance of 3.7 mm and with an SE detector.

The aggregation of PS-Pd NPs and PS NPs was measured at timepoints of 0 h and 24 h incubations by DLS with the Zetasizer Nano ZS (Malvern) (Figure S1c, Supporting Information). For this, PS-Pd NPs and PS NPs were incubated at 37° C in water and RPMI 1640 culture media supplemented with 10% fetal bovine serum (FBS). Samples were made in triplicates for underneath combinations in 6-well plates at a particle concentration of 500 μg mL^{-1}.

Peripheral Blood Mononuclear Cells Isolation and Culture: PBMCs were harvested from ethylenediamine tetraacetic acid (EDTA)-venous blood from informed, healthy donors (both females and males 25–50 years old) using a Ficoll-Paque (GE Healthcare, CA, USA) standard separation protocol. Informed signed consent was obtained from all the donors. Cell separation and experiments were performed immediately after the blood draw. PBMCs were cultured in 24-well plates in RPMI 1640 medium (Invitrogen, CA, USA), supplemented with 10% heat-inactivated FBS (Invitrogen, CA, USA) and 1% P/S (Life Technologies). At least 2×10^5 cells/sample in each experiment were used.

Cytotoxicity by Flow Cytometry: To evaluate the cytotoxicity of NPs, PBMCs were incubated with 50 μg mL^{-1} of NPs for 24 h. Ethanol at 70% was used as a positive control, while samples incubated with medium alone were used as negative controls. Cell viability of PBMCs was evaluated by staining with both Annexin V FITC (BD Biosciences) to detect apoptotic cells and Fixable Viability Stain 780 (BD Biosciences). Staining was performed in the dark for 20 min. Cells were processed by flow cytometry (FACS LRS Fortessa, BD Bioscience), and data were analyzed by FlowJo Software.

Cell Activation by Flow Cytometry: PBMC, THP1 (Cat# TIB-202, ATCC), and Jurkat (Cat# TIB-152, ATCC) activation were analyzed after treatment with diverse NPs (50 μg mL^{-1}) for 24 h. Cells were stained to identify immune activation markers. CD25 and CD69 (PE-conjugated anti-CD25, M-A251 clone; PE-Cy7-conjugated anti-CD69, FN50 clone; BD Bioscience, CA, USA) were used as activation markers. Staining was performed in the dark for 20 min. LPS (2 μg mL^{-1}, Sigma) was used as a positive control. Cells were processed by flow cytometry (FACS Canto II, BD Bioscience, CA, USA), and data were analyzed by FlowJo Software as previously reported.[97–99]

© 2024 The Author(s). Advanced Materials published by Wiley-VCH GmbH
RIGHTSLINK
15214095, 0, Downloaded from https://onlinelibrary.wiley.com/doi/10.1002/adma.202413413 by Ankara University Library, Wiley Online Library on [27/10/2024]. See the Terms and Conditions (https://onlinelibrary.wiley.com/terms-and-conditions) on Wiley Online Library for rules of use; OA articles are governed by the applicable Creative Commons License

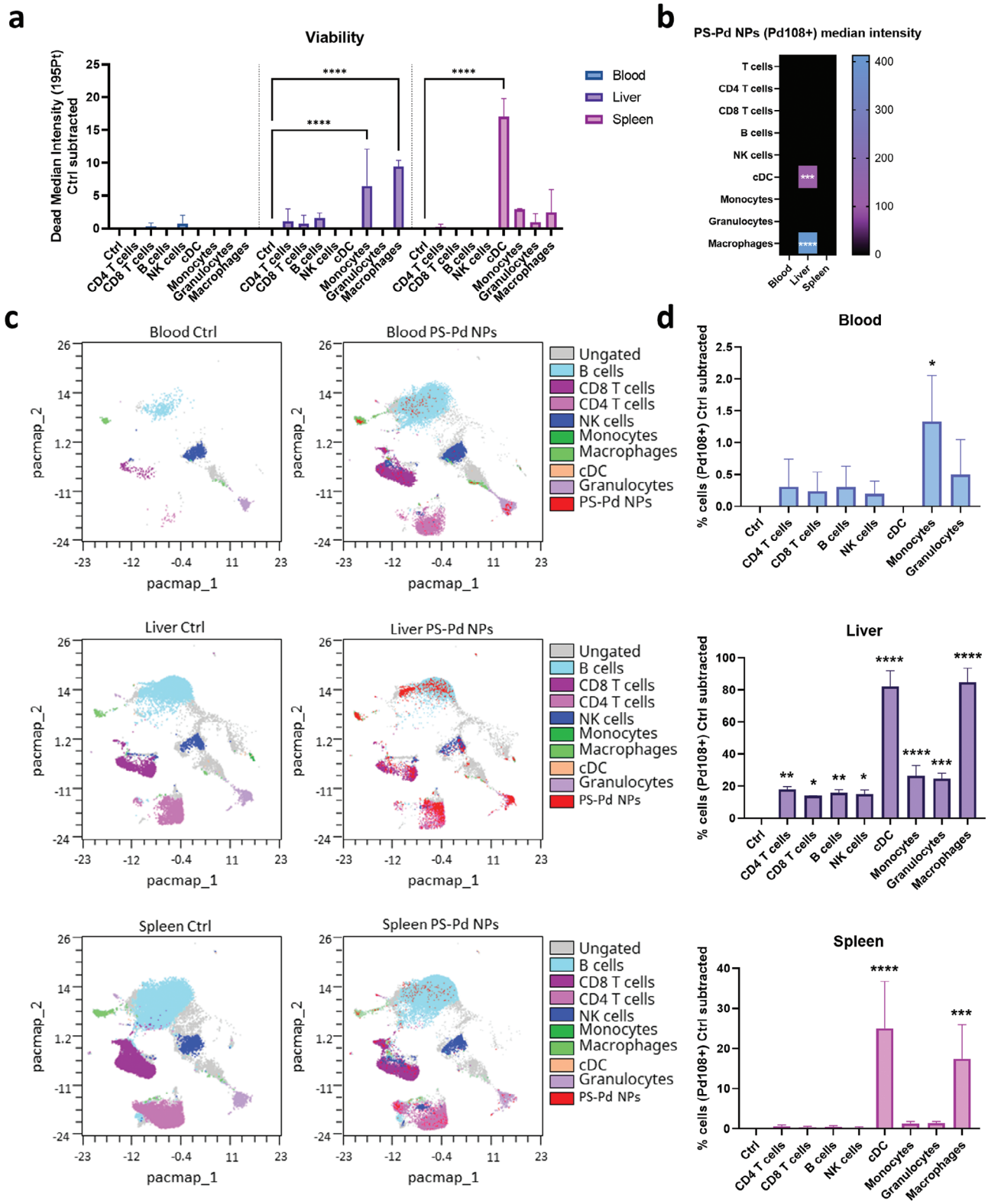


Figure 7. Biodistribution Study of 50 μg mL^{-1} PS-Pd Nanoparticles (NPs) in Major Immune Populations a) Impact on viability, comparison of cell viability between treated (50 μg mL^{-1} PS-Pd NPs) and untreated (Ctrl) samples in liver, blood, and spleen (N = 3). b) Detection of nanoparticle uptake in liver, blood, and spleen samples, showing the median intensity levels of PS-Pd NPs in Pd108+ channel. c) pacMAP visualization where red dots represent cells positive for PS-Pd NPs within major immune populations, demonstrating the distribution pattern. d) Quantification of PS-Pd NP-positive cells across major immune populations in liver, blood, and spleen samples. Data are presented as mean ± ST.D. of three independent samples. *$p < 0.05$; **$p < 0.01$; ***$p < 0.001$; ****$p < 0.0001$, by one-way ANOVA Tukey's multiple comparison test.

© 2024 The Author(s). Advanced Materials published by Wiley-VCH GmbH

15214095, 0, Downloaded from https://onlinelibrary.wiley.com/doi/10.1002/adma.202413413 by Ankara University Library, Wiley Online Library on [27/10/2024]. See the Terms and Conditions (https://onlinelibrary.wiley.com/terms-and-conditions) on Wiley Online Library for rules of use; OA articles are governed by the applicable Creative Commons License

ROS Detection Assay: To assess reactive oxygen species (ROS) levels in cultured cells, we employed the CellRox Green Flow Cytometry Assay Kit (Thermo Fisher Scientific). Cells were seeded in 6-well plates at a density of 1×10^6 cells per well and allowed to adhere overnight. The following day, cells were treated with various concentrations of the test compound for 24 h. After treatment, the medium was removed, and cells were washed twice with phosphate-buffered saline (PBS). Subsequently, cells were incubated with 500 µL of CellRox Green Reagent diluted in serum-free medium to a final concentration of 5 µM for 30 min at 37 °C in the dark. Following incubation, cells were trypsinized, collected, and washed twice with PBS. The cells were then resuspended in 500 µL of PBS for flow cytometric analysis. Fluorescence intensity was measured using a flow cytometer with excitation and emission wavelengths of 488 and 520 nm, respectively. Data were analyzed using flow cytometry software, and ROS levels were quantified as the mean fluorescence intensity of the cell population.

RNA Isolation and Sequencing: To perform the bulk RNA sequencing, 2×10^6 THP1 were treated or untreated with 50 µg mL^{-1} of PS-NPs for 24 h. After incubation, cells were lysed in 1 ml of TRIzol; following lysis, the aqueous phase was collected for RNA isolation after adding 200 µl of chloroform per ml of TRIzol. RNA isolation was performed using the QIACube instrument (Qiagen) with the Qiagen RNeasy Plus Micro Kit (cat# 74034). RNA quality was assessed using the Bioanalyzer 2100 (Agilent Technologies, Inc.), and all samples had an RNA Integrity Number (RIN) above 8. Library preparation was performed using the SMARTer Stranded Total RNA Sample Prep Kit (Takara Bio USA, Inc., cat# 634878). The library construction utilized total RNA with both RiboGone and SMART (Switching Mechanism At 5' end of RNA Template) technologies, along with PCR amplification, to generate Illumina-compatible libraries without the need for adapter ligations. RiboGone technology effectively depletes rRNA from total RNA samples prior to library generation. Library quality was assessed using the TapeStation 2000 instrument (Agilent Technologies), and the concentration was measured using Qubit (Thermo Fisher Scientific Inc.) before sequencing. Dual-indexed i5 and i7 paired-end libraries were sequenced on the NovaSeq 6000 system (Illumina, Inc.) with an average of 40 million reads per sample.

Proteomics Analysis: In this study, the effects of nanoplastics on THP-1 were investigated using a detailed proteomic analysis. Initially, proteins were extracted from the treated cells using appropriate lysis buffers. These proteins were then digested into peptides using trypsin. The peptides were separated and analyzed by high-resolution liquid chromatography-tandem mass spectrometry (LC-MS/MS), which involved the separation of peptides based on hydrophobicity, followed by their ionization and fragmentation to identify and quantify the proteins.

The mass spectrometry data were processed using advanced bioinformatics tools, allowing for the identification and quantification of proteins by matching the spectra against protein databases.[100] Quantitative analysis compared the protein abundances in nanoplastic-treated cells with control cells, highlighting molecular changes and specific biochemical pathways influenced by nanoplastic exposure.[101]

Transcriptomics and Proteomic Bioinformatic Analysis: The bioinformatics analysis started with transcriptome data, which underwent quality control using FastQC to check the raw sequencing reads. Next, we used Trimmomatic to trim off low-quality bases and adapters.[102] The cleaned reads were then aligned to the reference genome with HISAT2, known for its efficiency and sensitivity.[103] After that, HTSeq-count helped quantify gene expression by counting the reads mapped to each gene.[104] To identify differentially expressed genes, we used DESeq2, which offers robust statistical methods.[105] In parallel, both transcriptome and proteome data were processed to generate count files. These count files, alongside the transcriptome count files, were used for Gene Set Enrichment Analysis (GSEA) with the ReactomePA package.[106] This step was crucial for identifying significantly enriched biological pathways and processes.

To bring everything together and visualize the results, we switched to Python. We used Pandas for data manipulation, Seaborn and Matplotlib for advanced data visualization,[107,108] and Biopython for processing biological data.[109] This combination allowed for comprehensive analyses and clear visual representations of our data. This approach helped us effectively process and analyze the datasets, making the most of both R and Python's capabilities in bioinformatics.

Single-Cell Mass Cytometry Analysis of PS NP Impact: Single-cell mass cytometry analysis was performed on isolated PBMCs, collected as described above and seeded at a concentration of 4×10^6 cells $well^{-1}$ in 6-well plates. PBMCs were incubated with 50 µg mL^{-1} NPs for 24 h. LPS at 0.5 µg mL^{-1} (Sigma – Aldrich, Missouri, USA), EtOH 70%, and non-treated cells were selected, respectively, as positive and negative controls. 6 h prior to the treatment ending, cells were co-incubated with 10 µg mL^{-1} Brefeldin A (Invitrogen, CA, USA). After the incubation, PBMCs were washed with PBS supplemented with 0.5 M EDTA and 5% Fetal Bovine Serum (FBS).

Cells were then barcoded using Cell-ID 20-Plex Pd Barcoding Kit (Fluidigm, CA, USA). The barcoded samples were stained with Cell-ID Cisplatin (1:1000, Fluidigm, CA, USA), Maxpar Human Peripheral Blood Phenotyping, and Human Intracellular Cytokine I Panel Kits (Fluidigm, CA, USA) following the manufacturer instructions. To begin with, cells were fixed and permeabilized with 1X Fix I Buffer and 1X Barcode Perm Buffer, obtaining a uniform cell labeling with the palladium barcode. Thanks to the barcoding process, samples were pooled together and resuspended into a 5 ml polystyrene round-bottom tube using the Maxpar Cell Staining Buffer.

The surface marker antibody mix (1:100 dilutions for each antibody, final volume 800 µl) was added to the sample. Cells were then carefully mixed and incubated for 30 min at room temperature. At the end of the incubation, samples were washed twice with Maxpar Cell Staining Buffer and fixed by incubation with 1.6% paraformaldehyde for 10 min. After this, cells were washed twice with Maxpar Perm-S Buffer, centrifuged for 10 min at 1000×g, resuspended in 400 µl of Maxpar Perm-S Buffer, and incubated with cytoplasmic/secreted antibody mix for 30 min (1:100 dilutions for each antibody, final volume 800 µl). Following the incubation, cells were washed twice with Maxpar Cell Staining Buffer and stained overnight using 0.125 µM Cell-ID Intercalator-Ir solution. The day after, samples were washed twice with Maxpar Cell Staining Buffer, resuspended with 2 ml of Maxpar water, and filtered before data acquisition using a 0.22 µm cell strainer cap to remove possible cell clusters or aggregates. Data were analyzed using the mass cytometry platform CyTOF2 (Fluidigm Corporation, CA, USA).

In Vivo Biodistribution: For the in vivo biodistribution experiments, 3 male C57BL/6J (cat. #000664) mice per group were used. Mice were injected I.V. retro-orbitally with a 100 µL PS-NP (10 µg g−1 each in sterile PBS) or only sterile PBS. After 24 h, mice were euthanized by CO2 inhalation followed by blood withdrawal via cardiac puncture before further organ and tissue dissection. All experiments followed the guidelines of the Augusta University Animal Care and Use Committee. Approval for the use of rodents was obtained from Augusta University according to criteria outlined in the Guide for the Care and Use of Laboratory Animals from the National Institutes of Health. Blood, spleen, and livers were harvested, and single-cell suspension was isolated by established procedure.[58] The cell suspension for each organ was collected, washed with PBS, and kept on ice in PBS with 2% FBS until further staining and CyTOF analysis as described above. The antibody cocktail used is listed in Table S3, Supporting Information.

Gating strategy: CyTOF data analysis was performed as described before. Briefly, FCS files were normalized and analyzed by Cytobank. Doublets, cell debris, and dead cells were excluded through the gating strategy using Cell-ID Intercalator-Ir and LD. PBMC subsets and specific subpopulations were determined, as portrayed in Figure S3, Supporting Information. Specifically: T cells (CD45+ CD19- CD3+), Naïve Th. Cells (CD3+ CD4+ CD45RA+ CD27+ CD38− HLADR−), Effector Th. cells (CD3+ CD4+ CD45RA+ CD27− CD38− HLADR−), Activated Th. cells (CD3+ CD4+ CD38+ HLADR+), Naïve CT cells (CD3+ CD8+ CD45RA+ CD27+ CD38− HLADR−), Effector CT cells (CD3+ CD8+ CD45RA+ CD27− CD38− HLADR−), Activated CT cells (CD3+ CD8+ CD38+ HLADR+), Classical monocytes (CD45+ CD3− CD19− CD20− HLADR+ CD14+), Intermediate monocytes (CD45+ CD3− CD19− CD20− HLADR+ CD14dim CD16+), Non-classical monocytes (CD45+ CD3− CD19− CD20− CD11c- CD14- CD16+), mDCs (CD45+ CD3− CD19− CD20− CD14− HLA−

© 2024 The Author(s). Advanced Materials published by Wiley-VCH GmbH

15214095, 0, Downloaded from https://onlinelibrary.wiley.com/doi/10.1002/adma.202413413 by Ankara University Library, Wiley Online Library on [27/10/2024]. See the Terms and Conditions (https://onlinelibrary.wiley.com/terms-and-conditions) on Wiley Online Library for rules of use; OA articles are governed by the applicable Creative Commons License

DR+ CD11c+ CD123−), pDCs) (CD45+ CD3− CD19− CD20− CD14− CD11c− HLADR+ CD123+), NK cells (CD45+ CD3− CD19− CD20− CD14− CD11c- CD38+ CD16+), B cells (CD3- CD20+ CD19+), Naïve B cells (CD27−), Plasma B cells (HLADR- CD38+). The heat map visualization created with Cytobank allowed the comparison between the marker fluorescence of the treated populations with mean fluorescent intensity toward the untreated control. Moreover, viSNE, a Cytobank tool implemented for cytometry analysis, was employed. The t-stochastic neighbor embedding (t-SNE) shows single cells in a 2- or 3D plot based on their relationships. To characterize the viSNE map, ten cell surface markers were used (i.e., CD3, CD4, CD8a, CD11c, CD14, CD16, CD19, CD20, CD123, and HLA-DR).

Cytokine data were analyzed using the viSNE tool and displayed as plots of the expression intensity of the studied cytokines (i.e., IL-6, IL-2, IL-17a, IFN-γ, Mip1b, GrB, HLA-DR, and Perforin), and heat maps of mean marker expression ratio for cytokines that displayed modulations upon treatment with NPs.

Detection of NP Cell Uptake by TEM: For TEM analysis, samples were fixed with 2.5% glutaraldehyde in 0.1M sodium cacodylate buffer pH 7.4 ON at 4 °C. The samples were postfixed with 1% osmium tetroxide plus potassium ferrocyanide 1% in 0.1 M sodium cacodylate buffer for 1 h at 4 °C. After three water washes, samples were dehydrated in a graded ethanol series and embedded in an epoxy resin (Sigma-Aldrich). Ultrathin sections (60–70 nm) were obtained with an Ultrotome V (LKB) ultramicrotome, counterstained with uranyl acetate and lead citrate, and viewed with a Tecnai G^2 (FEI) transmission electron microscope operating at 100 kV. Images were captured with a Veleta (Olympus Soft Imaging System) digital camera.

PS-Pd NP Quantification Determined by CyTOF Solution Mode: The dynamic range of $^{102-110}$Pd was determined by CyTOF solution mode. The dynamic range of Pd was evaluated by mass cytometry CyTOF Helios system at Fluidigm Canada, solution mode). PS-Pd NPs 200nm (50 µg/mL^{-1}) solutions were diluted 1:3 to create a calibration curve (0.00, 0.0076, 0.023, 0.068, 0.2, 0.61, 1.85, 5.55, 16.6, and 50 µg mL^{-1}).

Number of NPs per Cell Calculation: The mean ^{108}Pd ion intensity within a specific cell population measured by mass cytometry is addressed as the 'mean dual counts.' This value is proportional to the number of ^{108}Pd atoms per cell, and it is the product of the integral over time of detector intensity multiplied by the dual count coefficient of ^{108}Pd.

The conversion of dual counts to the number of palladium atoms per cell was determined using the calculations reported by Yang *et al.*, Nat com, 2017 as follows:

$$\text{Number of}\,^{108}\text{Pd atoms per cell} = {}^{108}\text{Pd}/{}^{193}\text{Ir transmission factor} \quad (1)$$

Since the transmission coefficient for ^{108}Pd cannot be directly assessed in the cytometer but can be measured for ^{193}Ir, characterized by a degree of ionization similar to the one of PS-Pd NPs (Iridium and Palladium have ionization energies of 8.9670 (^{193}Ir), 8.3369 (^{108}Pd) eV, respectively). The ^{193}Ir transmission coefficient was calculated by dividing the dual counts of ^{193}Ir detected for the instrument tuning solution by the number of ^{193}Ir atoms introduced in the 0.25 p.p.b. Ir tuning solution (Fluidigm CAT#201072) as reported below:

$$^{193}Ir\ transmission\ factor = \frac{^{193}Ir\ dual\ counts}{(Ir\ atoms\ introduced) * (^{193}Ir\ natural\ abundance)} = \frac{^{193}Ir\ dual\ counts}{^{193}Ir\ atoms\ introduced} = \frac{(Ir\ concentration)(flow\ rate)(integration\ time)(natural\ abundance)(Avogadros\ number)}{Isotope\ mass}$$

Using the variables tuning solution Ir concentration (2.5 × 10^{-13} g µL^{-1}), flow rate (0.75 µL s^{-1} for CyTOF2 or 0.5 µL s^{-1} for Helios), the integration time (CyTOF2: 2.666 s; Helios: 4 s), the natural abundance of ^{193}Ir (0.627), Avogadro's number 6.02 × 10^{23}, and isotope mass (193 g mol^{-1}). Finally, the number of associated NPs per cell was calculated by the number of atoms per cell divided by the number of atoms per NP.

Hemolysis Assay: 100 µL of fresh human whole blood (1×10^6 cells) was harvested from informed, healthy donors (25–50 years old) using a Ficoll-Paque (GE Healthcare, CA, USA) standard separation protocol. Informed signed consent was obtained from all the donors. The Ethics Committee of the University of Padua reviewed and approved all the protocols performed. Blood was stabilized with ethylenediamine tetraacetic acid (EDTA). Serum was removed from blood samples by centrifugation at 200 g for 5 min. RBCs were washed three times and then diluted with sterile isotonic PBS. To determine the hemolytic activity, NPs (50 µg mL^{-1}) were added to RBCs suspension in a final volume of 1mL PBS. After vortexing, the mixtures were left at 37 °C in a Thermo mixer at 500/600g for 1 and 24h. At the end of the incubation times, RBCs were removed by centrifugation. A microplate reader (Sunrise TECAN Infinite M200PRO) measured the absorbance of the hemoglobin in the supernatant at 570 nm, with the absorbance at 620 nm as a reference.

High-Dimensional Immune Profiling of Human Whole Blood: Whole blood was collected from healthy donors (25–50 years old). 500 µl of whole blood was incubated with 50 µg mL^{-1} of PS-Pd NPs for 24 h at 37 °C, 5 vol. % CO_2. Post-incubation Maxpar Direct Immune Profiling Assay (MDIPA) was performed by aliquoting 270 µl of whole blood into a tube containing ready-to-use dry-format 30-antibody staining, as reported in Table S4, Supporting Information. Samples were stained for 30 min at room temperature in the dark. After the antibody staining, red blood cells (RBCs) were lysed with Cal-lyse buffer for 10 min in the dark (Thermo Fisher Scientific, Waltham, MA) and then washed with Cell Staining Buffer (Fluidigm, San Francisco, CA, USA). After this, cells were fixed with Maxpar Fix I buffer, washed twice with Maxpar Perm-S Buffer, centrifuged for 10 min at 1000 ×g, resuspended in 400 µl of Maxpar Perm-S Buffer, and incubated with the following antibodies: anti-human IL4-^{142}Nd, anti-human INFy-^{165}Ho, anti-human TNFα-^{175}Lu, anti-human GM-CSF-^{159}Tb (Fluidigm, San Francisco, CA, USA) for 30 min (1:100 dilutions for each antibody, final volume 800 µl). Samples were fixed with 1.6% formaldehyde, incubated for 10 min, washed with Cell Staining Buffer (Fluidigm, San Francisco, CA, USA), and stained overnight with Cell-ID Intercalator-Ir (Fluidigm, San Francisco, CA, USA) diluted in Fix Perm Buffer (Fluidigm, San Francisco, CA, USA) for a final concentration of 125nM. Each sample was washed twice with Maxpar Cell Staining Buffer and suspended with 2 ml of ultra-pure water. Before the data acquisition, each sample was filtered into 5 ml round bottom polystyrene tubes with a 30 µm cell strainer cap to remove possible cell clusters or aggregates. Data were analyzed using the mass cytometry platform CyTOF2 (Fluidigm Corporation, CA, USA). All experiments were performed in biological and technical triplicate. Phenotyping and Cytokine data were analyzed using the Pathsetter program and following the gating strategy reported in Figure S11, Supporting Information. The studied cytokines (i.e.) IL-4, IFNγ, TNFα, and GMCSF heat maps of mean marker expression ratio displayed modulations upon NPs treatment.

Statistical Analysis: All values are expressed as mean ± ST.D. Comparison between groups was performed by either two-way or one-way ANOVA, followed by Tukey's post hoc multiple comparison, where data were normally distributed. Kruskall-Wallis ANOVA statistically analyzed data that did not follow the normal distribution. ROS detection was statistically analyzed by Mann-Whitney U-test. Comparisons between the two groups were performed using a two-tailed Student's *t*-test. At least three independent samples were analyzed. A value of $p < 0.05$ was considered significant.

Supporting Information

Supporting Information is available from the Wiley Online Library or from the author.

Acknowledgements

L.F., A.G., and L.G. equal contribution L.G.D. conceived the study and coordinated the work. L.G.D., L.F., A.G., and MO wrote the manuscript with input from all the other authors. D.M.M. synthesized the Pd-doped nanoplastics. R.B.S. characterized the NPs and performed the agglomeration studies. L.F., A.G., M.O., L.G. R.U. O.B., D.C., and M.Z. performed the experiments and analyzed the data. L.G.D., L.F., A.G., M.O., and A.Y. interpreted the experimental data, to which all authors contributed. All

© 2024 The Author(s). Advanced Materials published by Wiley-VCH GmbH

RIGHTSLINK

15214095, 0, Downloaded from https://onlinelibrary.wiley.com/doi/10.1002/adma.202413413 by Ankara University Library, Wiley Online Library on [27/10/2024]. See the Terms and Conditions (https://onlinelibrary.wiley.com/terms-and-conditions) on Wiley Online Library for rules of use; OA articles are governed by the applicable Creative Commons License

co-authors approved the final version of the present manuscript. The authors acknowledge the funding from the STARS Consolidator Grant (DETECTION), the European Union's Horizon Europe program under the Marie Sklodowska-Curie grant agreement No. 101086184 (MX-MAP) and the Erasmus+ project 2022-1-TR01-KA-VET-000088373 (A UNIVERSAL STRATEGIC NECESSITY: FROM MOLECULE TO DRUG). L.G.D. and L.F. acknowledge funding from the European Union's Horizon 2020 Research and Innovation Programme under Marie Sklodowska-Curie Grant Agreement No. 101029140 (SEE). M.O. and L.G.D. want to thank Jiji Xie and the Flow and Mass Cytometry Core at the Georgia Cancer Center, Augusta University, for their support. D.M.M and R.B.S. were funded by the Swiss National Science Foundation, Project number PCEFP2_186856.

Open access publishing facilitated by Universita degli Studi di Padova, as part of the Wiley - CRUI-CARE agreement.

Conflict of Interest

The authors declare no conflict of interest.

Data Availability Statement

The data that support the findings of this study are available from the corresponding author upon reasonable request.

Keywords

biocompatibility, blood exposure, CyTOF, immune cells, pollution, safety

Received: September 6, 2024
Revised: October 7, 2024
Published online:

[1] World Economic Forum, Ellen MacArthur Foundation and McKinsey & Company, The New Plastics Economy: Rethinking the future of plastics (**2016**).
[2] "The New Plastics Economy: Rethinking the future of plastics," can be found under https://ellenmacarthurfoundation.org/the-new-plastics-economy-rethinking-the-future-of-plastics.
[3] J. A. Brandon, W. Jones, M. D. Ohman, *Sci. Adv.* **2019**, *5*, aax058
[4] S. Allen, D. Allen, V. R. Phoenix, G. Le Roux, P. Durántez Jiménez, A. Simonneau, S. Binet, D. Galop, *Nat. Geosci.* **2019**, *12*, 339.
[5] M. S. Savoca, M. E. Wohlfeil, G. A. Nevitt, *Sci. Adv.* **2016**, *2*, 1600395
[6] M. Eriksen, L. C. M. Lebreton, H. S. Carson, M. Thiel, C. J. Moore, J. C. Borerro, F. Galgani, P. G. Ryan, J. Reisser, *PLoS One* **2014**, *9*, e111913.
[7] C. Wilcox, N. J. Mallos, G. H. Leonard, A. Rodriguez, B. D. Hardesty, *Mar. Policy* **2016**, *65*, 107.
[8] A. Amobonye, P. Bhagwat, S. Raveendran, S. Singh, S. Pillai, *Front. Microbiol.* **2021**, *12*, 768297.
[9] J. Gigault, A. ter Halle, M. Baudrimont, P.-Y. Pascal, F. Gauffre, T.-L. Phi, H. El Hadri, B. Grassl, S. Reynaud, *Environ. Pollut.* **2018**, *235*, 1030.
[10] N. B. Hartmann, T. Hüffer, R. C. Thompson, M. Hassellöv, A. Verschoor, A. E. Daugaard, S. Rist, T. Karlsson, N. Brennholt, M. Cole, M. P. Herrling, M. C. Hess, N. P. Ivleva, A. L. Lusher, M. Wagner, *Environ. Sci. Technol.* **2019**, *53*, 1039.
[11] D. M. Mitrano, P. Wick, B. Nowack, *Nat. Nanotechnol.* **2021**, *16*, 491.
[12] E. S. Gruber, V. Stadlbauer, V. Pichler, K. Resch-Fauster, A. Todorovic, T. C. Meisel, S. Trawoeger, O. Hollóczki, S. D. Turner, W. Wadsak, A. D. Vethaak, L. Kenner, *Exposure Health* **2022**, *15*, 33.
[13] A. D. Vethaak, J. Legler, *Science* **2021**, *371*, 672.
[14] A. A. Koelmans, P. E. Redondo-Hasselerharm, N. H. M. Nor, V. N. de Ruijter, S. M. Mintenig, M. Kooi, *Nat. Rev. Mater.* **2022**, *7*, 138.
[15] T. S. Galloway, M. Cole, C. Lewis, *Nat. Ecol. Evol.* **2017**, *1*, 116.
[16] A. A. de Souza Machado, W. Kloas, C. Zarfl, S. Hempel, M. C. Rillig, *Glob. Chang. Biol.* **2018**, *24*, 1405.
[17] S. Wagner, T. Reemtsma, *Nat. Nanotechnol.* **2019**, *14*, 300.
[18] T. P. Haider, C. Völker, J. Kramm, K. Landfester, F. R. Wurm, *Angew. Chem., Int. Ed.* **2019**, *58*, 50.
[19] X. Kong, A. A. Koelmans, *Environ. Sci. Technol.* **2019**, *53*, 13822.
[20] S. L. Wright, J. Ulke, A. Font, K. L. A. Chan, F. J. Kelly, *Environ Int* **2020**, *136*, 105411.
[21] J. C. Prata, J. P. da Costa, I. Lopes, A. C. Duarte, T. Rocha-Santos, *Sci. Total Environ.* **2020**, *702*, 134455.
[22] B. Toussaint, B. Raffael, A. Angers-Loustau, D. Gilliland, V. Kestens, M. Petrillo, I. M. Rio-Echevarria, G. Van den Eede, *Food Addit. Contam., Part A* **2019**, *36*, 639.
[23] M. Carbery, W. O'Connor, T. Palanisami, *Environ. Int.* **2018**, *115*, 400.
[24] Y. Chae, D. Kim, S. W. Kim, Y.-J. An, *Sci. Rep.* **2018**, *8*, 284.
[25] H. A. Leslie, M. J. M. van Velzen, S. H. Brandsma, A. D. Vethaak, J. J. Garcia-Vallejo, M. H. Lamoree, *Environ. Int.* **2022**, *163*, 107199.
[26] A. Banerjee, W. L. Shelver, *Sci. Total Environ.* **2021**, *755*, 142518.
[27] B. Prietl, C. Meindl, E. Roblegg, T. R. Pieber, G. Lanzer, E. Fröhlich, *Cell Biol. Toxicol.* **2014**, *30*, 1.
[28] G. F. Schirinzi, I. Pérez-Pomeda, J. Sanchís, C. Rossini, M. Farré, D. Barceló, *Environ. Res.* **2017**, *159*, 579.
[29] J. Hwang, D. Choi, S. Han, J. Choi, J. Hong, *Sci. Total Environ.* **2019**, *684*, 657.
[30] C. Q. Y. Yong, S. Valiyaveettil, B. L. Tang, *Int. J. Environ. Res. Public Health* **2020**, *17*, 1509.
[31] M. Bonanomi, N. Salmistraro, D. Porro, A. Pinsino, A. M. Colangelo, D. Gaglio, *Chemosphere* **2022**, *303*, 134947.
[32] J. Hwang, D. Choi, S. Han, S. Y. Jung, J. Choi, J. Hong, *Sci. Rep.* **2020**, *10*, 7391.
[33] A. Brewer, I. Dror, B. Berkowitz, *ACS EST Water* **2021**, *1*, 48.
[34] Z. Sobhani, X. Zhang, C. Gibson, R. Naidu, M. Megharaj, C. Fang, *Water Res.* **2020**, *174*, 115658.
[35] Y. Yang, J. Wang, M. Xia, *Sci. Total Environ.* **2020**, *708*, 135233.
[36] O. Keinänen, E. J. Dayts, C. Rodriguez, S. M. Sarrett, J. M. Brennan, M. Sarparanta, B. M. Zeglis, *Sci. Rep.* **2021**, *11*, 11463.
[37] E. Fröhlich, C. Meindl, E. Roblegg, B. Ebner, M. Absenger, T. R. Pieber, *Part. Fibre Toxicol.* **2012**, *9*, 26.
[38] B. J. Teubl, B. Stojkovic, D. Docter, E. Pritz, G. Leitinger, I. Poberaj, R. Prassl, R. H. Stauber, E. Fröhlich, J. G. Khinast, E. Roblegg, *Clin. Oral Investig.* **2018**, *22*, 929.
[39] E. G. Karakolis, B. Nguyen, J. B. You, C. M. Rochman, D. Sinton, *Environ. Sci. Technol. Lett.* **2019**, *6*, 334.
[40] S. Liu, E. Shang, J. Liu, Y. Wang, N. Bolan, M. B. Kirkham, Y. Li, *Front Environ Sci Eng* **2021**, *16*, 8.
[41] S. Mariano, S. Tacconi, M. Fidaleo, M. Rossi, L. Dini, *Front. Toxicol.* **2021**, *3*, 636640.
[42] H. Maxwell S, F. Melinda K, G. Matthew, *Environ. Sci. Technol.* **2020**, *54*, 5580.
[43] Q. Gao, Y. Wang, Y. Ji, X. Zhao, P. Zhang, L. Chen, *J. Hazard. Mater.* **2022**, *424*, 127628.
[44] A. I. Catarino, A. Frutos, T. B. Henry, *Sci. Total Environ.* **2019**, *670*, 915.
[45] C. Schür, S. Rist, A. Baun, P. Mayer, N. B. Hartmann, M. Wagner, *Environ. Toxicol. Chem.* **2019**, *38*, 1495.
[46] D. M. Mitrano, A. Beltzung, S. Frehland, M. Schmiedgruber, A. Cingolani, F. Schmidt, *Nat. Nanotechnol.* **2019**, *14*, 362.
[47] M. Schmiedgruber, R. Hufenus, D. M. Mitrano, *Water Res.* **2019**, *155*, 423.

© 2024 The Author(s). Advanced Materials published by Wiley-VCH GmbH

RIGHTSLINK

15214095, 0, Downloaded from https://onlinelibrary.wiley.com/doi/10.1002/adma.202413413 by Ankara University Library, Wiley Online Library on [27/10/2024]. See the Terms and Conditions (https://onlinelibrary.wiley.com/terms-and-conditions) on Wiley Online Library for rules of use; OA articles are governed by the applicable Creative Commons License

[48] A. S. Keller, J. Jimenez-Martinez, D. M. Mitrano, *Environ. Sci. Technol.* **2020**, *54*, 911.
[49] S. Frehland, R. Kaegi, R. Hufenus, D. M. Mitrano, *Water Res.* **2020**, *182*, 115860.
[50] F. Ribeiro, D. M. Mitrano, C. Hacker, P. Cherek, K. Brigden, S. L. Kaserzon, K. V. Thomas, T. S. Galloway, *Environ. Sci. Technol.* **2022**, *56*, 16716.
[51] L. Hendriks, V. M. Kissling, T. Buerki-Thurnherr, D. M. Mitrano, *Environ. Sci.: Nano* **2023**, *10*, 3439.
[52] R. Gadalla, B. Noamani, B. L. MacLeod, R. J. Dickson, M. Guo, W. Xu, S. Lukhele, H. J. Elsaesser, A. R. A. Razak, N. Hirano, T. L. McGaha, B. Wang, M. Butler, C. J. Guidos, P. S. Ohashi, L. L. Siu, D. G. Brooks, *Front Oncol* **2019**, *9*, 00415.
[53] M. H. Spitzer, G. P. Nolan, *Cell* **2016**, *165*, 780.
[54] E. Galli, E. Friebel, F. Ingelfinger, S. Unger, N. G. Núñez, B. Becher, *Eur. J. Immunol.* **2019**, *49*, 212.
[55] D. J. Kunz, T. Gomes, K. R. James, *Front. Immunol.* **2018**, *9*, 01435.
[56] M. Orecchioni, D. Bedognetti, L. Newman, C. Fuoco, F. Spada, W. Hendrickx, F. M. Marincola, F. Sgarrella, A. F. Rodrigues, C. Ménard-Moyon, G. Cesareni, K. Kostarelos, A. Bianco, L. G. Delogu, *Nat. Commun.* **2017**, *8*, 1109.
[57] M. Orecchioni, V. Bordoni, C. Fuoco, G. Reina, H. Lin, M. Zoccheddu, A. Yilmazer, B. Zavan, G. Cesareni, D. Bedognetti, A. Bianco, L. G. Delogu, *Small* **2020**, *16*, 2070117.
[58] L. Fusco, A. Gazzi, C. E. Shuck, M. Orecchioni, D. Alberti, S. M. D'Almeida, D. Rinchai, E. Ahmed, O. Elhanani, M. Rauner, B. Zavan, J.-C. Grivel, L. Keren, G. Pasqual, D. Bedognetti, K. Ley, Y. Gogotsi, L. G. Delogu, *Adv. Mater.* **2022**, *34*, 2205154.
[59] A. Banerjee, L. O. Billey, W. L. Shelver, *PLoS One* **2021**, *16*, e0260803.
[60] X. Shi, X. Wang, R. Huang, C. Tang, C. Hu, P. Ning, F. Wang, *Int. J. Nanomed.* **2022**, *17*, 4509.
[61] Y.-Y. Lu, H. Li, H. Ren, X. Zhang, F. Huang, D. Zhang, Q. Huang, X. Zhang, *J. Hazard. Mater.* **2022**, *421*, 126770.
[62] O. Lunov, T. Syrovets, C. Loos, J. Beil, M. Delacher, K. Tron, G. U. Nienhaus, A. Musyanovych, V. Mailänder, K. Landfester, T. Simmet, *ACS Nano* **2011**, *5*, 1657.
[63] Y. Li, M. Xu, Z. Zhang, G. Halimu, Y. Li, Y. Li, W. Gu, B. Zhang, X. Wang, *J. Hazard. Mater.* **2022**, *424*, 127508.
[64] A. Weber, A. Schwiebs, H. Solhaug, J. Stenvik, A. M. Nilsen, M. Wagner, B. Relja, H. H. Radeke, *Environ Int* **2022**, *163*, 107173.
[65] D. Frasca, M. Romero, A. Diaz, S. Alter-Wolf, M. Ratliff, A. M. Landin, R. L. Riley, B. B. Blomberg, *J. Immunol.* **2012**, *188*, 279.
[66] A. S. Shanbhag, J. J. Jacobs, J. Black, J. O. Galante, T. T. Glant, *J. Orthop. Res.* **1995**, *13*, 792.
[67] R. B. Schefer, A. Armanious, D. M. Mitrano, *Environ. Sci. Technol.* **2023**, *57*, 14707.
[68] B. Rothen-Rutishauser, C. Mühlfeld, F. Blank, C. Musso, P. Gehr, *Part. Fibre Toxicol.* **2007**, *4*, 9.
[69] P. Foroozandeh, A. A. Aziz, *Nanoscale Res. Lett.* **2018**, *13*, 339.
[70] L. Shang, K. Nienhaus, G. U. Nienhaus, *J. Nanobiotechnol.* **2014**, *12*, 5.
[71] N. Hoshyar, S. Gray, H. Han, G. Bao, *Nanomedicine (Lond)* **2016**, *11*, 673.
[72] E.-H. Kim, S. Choi, D. Kim, H. J. Park, Y. Bian, S. H. Choi, H. Y. Chung, O.-N. Bae, *Part. Fibre Toxicol.* **2022**, *19*, 60.
[73] D. K. Sarma, R. Dubey, R. M. Samarth, S. Shubham, P. Chowdhury, M. Kumawat, V. Verma, R. R. Tiwari, M. Kumar, *Nanomaterials* **2022**, *12*, 1632.
[74] M. Panizzolo, V. H. Martins, F. Ghelli, G. Squillacioti, V. Bellisario, G. Garzaro, D. Bosio, N. Colombi, R. Bono, E. Bergamaschi, *Ecotoxicol. Environ. Saf.* **2023**, *267*, 115645.
[75] M. R. McLoughlin, D. J. Orlicky, J. R. Prigge, P. Krishna, E. A. Talago, I. R. Cavigli, S. Eriksson, C. G. Miller, J. A. Kundert, V. I. Sayin, R. A. Sabol, J. Heinemann, L. O. Brandenberger, S. V. Iverson, B. Bothner, T. Papagiannakopoulos, C. T. Shearn, E. S. J. Arnér, E. E. Schmidt, *Proc. Natl. Acad. Sci. U S A* **2019**, *116*, 11408.
[76] S. Nóbrega-Pereira, P. J. Fernandez-Marcos, T. Brioche, M. C. Gomez-Cabrera, A. Salvador-Pascual, J. M. Flores, J. Viña, M. Serrano, *Nat. Commun.* **2016**, *7*, 10894.
[77] Z. Rao, S. Wang, J. Wang, *Biomed. Pharmacother.* **2017**, *90*, 414.
[78] J. Zhang, Y. Guo, X. Zhao, J. Pang, C. Pan, J. Wang, S. Wei, X. Yu, C. Zhang, Y. Chen, H. Yin, F. Xu, *Nat. Rev. Cardiol.* **2023**, *20*, 495.
[79] C.-H. Chen, G. R. Budas, E. N. Churchill, M.-H. Disatnik, T. D. Hurley, D. Mochly-Rosen, *Science* **2008**, *321*, 1493.
[80] C. A. Neumann, D. S. Krause, C. V. Carman, S. Das, D. P. Dubey, J. L. Abraham, R. T. Bronson, Y. Fujiwara, S. H. Orkin, R. A. Van Etten, *Nature* **2003**, *424*, 561.
[81] T.-H. Kim, P. Leslie, Y. Zhang, *OncoTargets Ther.* **2014**, *5*, 860.
[82] S. J. Cameron, J. Sheng, F. Hosseinian, W. G. Willmore, *Int. J. Mol. Sci.* **2022**, *23*, 7962.
[83] P. Kumari, A. J. Russo, S. Shivcharan, V. A. Rathinam, *Immunol. Rev.* **2020**, *297*, 83.
[84] X. Gao, G. Wu, M. S.-M. Tsang, D. Huang, C. W.-K. Lam, C. K. Wong, *Cell Mol. Immunol.* **2022**, *19*, 1322.
[85] S. Schütze, V. Tchikov, W. Schneider-Brachert, *Nat. Rev. Mol. Cell Biol.* **2008**, *9*, 655.
[86] L. Flanagan, J. Sebastià, L. P. Tuffy, A. Spring, A. Lichawska, M. Devocelle, J. H. M. Prehn, M. Rehm, *Cell Death Dis.* **2010**, *1*, e49.
[87] S. Goyama, J. Schibler, L. Cunningham, Y. Zhang, Y. Rao, N. Nishimoto, M. Nakagawa, A. Olsson, M. Wunderlich, K. A. Link, B. Mizukawa, H. L. Grimes, M. Kurokawa, P. P. Liu, G. Huang, J. C. Mulloy, *J. Clin. Invest.* **2013**, *123*, 3876.
[88] S. A. Demir, Z. K. Timur, N. Ateş, L. A. Martínez, V. Seyrantepe, *J. Neuroinflammation* **2020**, *17*, 277.
[89] N. Hug, D. Longman, J. F. Cáceres, *Nucleic Acids Res.* **2016**, *44*, 1483.
[90] I. Voskoboinik, J. C. Whisstock, J. A. Trapani, *Nat. Rev. Immunol.* **2015**, *15*, 388.
[91] A. C. Wensink, V. Kemp, J. Fermie, M. I. García Laorden, T. van der Poll, C. E. Hack, N. Bovenschen, *Proc. Natl. Acad. Sci. USA* **2014**, *111*, 5974.
[92] A. Schmidt, W. A. da Silva Brito, D. Singer, M. Mühl, J. Berner, F. Saadati, C. Wolff, L. Miebach, K. Wende, S. Bekeschus, *Part. Fibre Toxicol.* **2023**, *20*, 3.
[93] R. Gautam, J. Jo, M. Acharya, A. Maharjan, D. Lee, P. B. K. C., C. Kim, K. Kim, H. Kim, Y. Heo, *Sci. Total Environ.* **2022**, *838*, 156089.
[94] M. Kumar, P. Kulkarni, S. Liu, N. Chemuturi, D. K. Shah, *Adv. Drug Delivery Rev.* **2023**, *194*, 114708.
[95] L. Yang, H. Kuang, W. Zhang, Z. P. Aguilar, H. Wei, H. Xu, *Sci. Rep.* **2017**, *7*, 3303.
[96] J. Bourquin, A. Milosevic, D. Hauser, R. Lehner, F. Blank, A. Petri-Fink, B. Rothen-Rutishauser, *Adv. Mater.* **2018**, *30*, 1704307.
[97] E. Avitabile, L. Fusco, S. Minardi, M. Orecchioni, B. Zavan, A. Yilmazer, M. Rauner, P. Pippia, E. Tasciotti, L. G. Delogu, *Front. Bioeng. Biotechnol.* **2020**, *8*.
[98] V. Bordoni, G. Reina, M. Orecchioni, G. Furesi, S. Thiele, C. Gardin, B. Zavan, G. Cuniberti, A. Bianco, M. Rauner, L. G. Delogu, *Nanoscale* **2019**, *11*, 19408.
[99] J. Russier, V. León, M. Orecchioni, E. Hirata, P. Virdis, C. Fozza, F. Sgarrella, G. Cuniberti, M. Prato, E. Vázquez, A. Bianco, L. G. Delogu, *Angew. Chem., Int. Ed.* **2017**, *56*, 3014.
[100] E. Kirbas Cilingir, O. Besbinar, L. Giro, M. Bartoli, J. L. Hueso, K. J. Mintz, Y. Aydogan, J. M. Garber, M. Turktas, O. Ekim, A. Ceylan, M. A. Unal, M. Ensoy, F. Arı, O. Ozgenç Çinar, B. I. Ozturk, C. Gokce, D. Cansaran-Duman, M. Braun, J. Wachtveitl, J. Santamaria, L. G. Delogu, A. Tagliaferro, A. Yilmazer, R. M. Leblanc, *Small* **2024**, *20*, 2309283.

© 2024 The Author(s). Advanced Materials published by Wiley-VCH GmbH

RIGHTSLINK
15214095, 0, Downloaded from https://onlinelibrary.wiley.com/doi/10.1002/adma.202413413 by Ankara University Library, Wiley Online Library on [27/10/2024]. See the Terms and Conditions (https://onlinelibrary.wiley.com/terms-and-conditions) on Wiley Online Library for rules of use; OA articles are governed by the applicable Creative Commons License

[101] H. Taheri, M. A. Unal, M. Sevim, C. Gurcan, O. Ekim, A. Ceylan, Z. Syrgiannis, K. C. Christoforidis, S. Bosi, O. Ozgenç, M. J. Gómez, M. Turktas Erken, Ç. Soydal, Z. Eroğlu, C. V. Bitirim, U. Cagin, F. Arı, A. Ozen, O. Kuçuk, L. G. Delogu, M. Prato, Ö. Metin, A. Yilmazer, *Small* **2020**, *16*, 1904619.
[102] A. M. Bolger, M. Lohse, B. Usadel, *Bioinformatics* **2014**, *30*, 2114.
[103] D. Kim, B. Langmead, S. L. Salzberg, *Nat. Methods* **2015**, *12*, 357.
[104] S. Anders, P. T. Pyl, W. Huber, *Bioinformatics* **2015**, *31*, 166.
[105] M. I. Love, W. Huber, S. Anders, *Genome Biol.* **2014**, *15*, 550.
[106] G. Yu, L.-G. Wang, Y. Han, Q.-Y. He, *OMICS* **2012**, *16*, 284.
[107] M. Waskom, *J. Open Source Software* **2021**, *6*, 3021.
[108] J. Hunter, *Comput. Sci. Eng.* **2007**, *9*, 90.
[109] P. J. A. Cock, T. Antao, J. T. Chang, B. A. Chapman, C. J. Cox, A. Dalke, I. Friedberg, T. Hamelryck, F. Kauff, B. Wilczynski, M. J. L. de Hoon, *Bioinformatics* **2009**, *25*, 1422.

© 2024 The Author(s). Advanced Materials published by Wiley-VCH GmbH

RIGHTSLINK

15214095, 0, Downloaded from https://onlinelibrary.wiley.com/doi/10.1002/adma.202413413 by Ankara University Library, Wiley Online Library on [27/10/2024]. See the Terms and Conditions (https://onlinelibrary.wiley.com/terms-and-conditions) on Wiley Online Library for rules of use; OA articles are governed by the applicable Creative Commons License